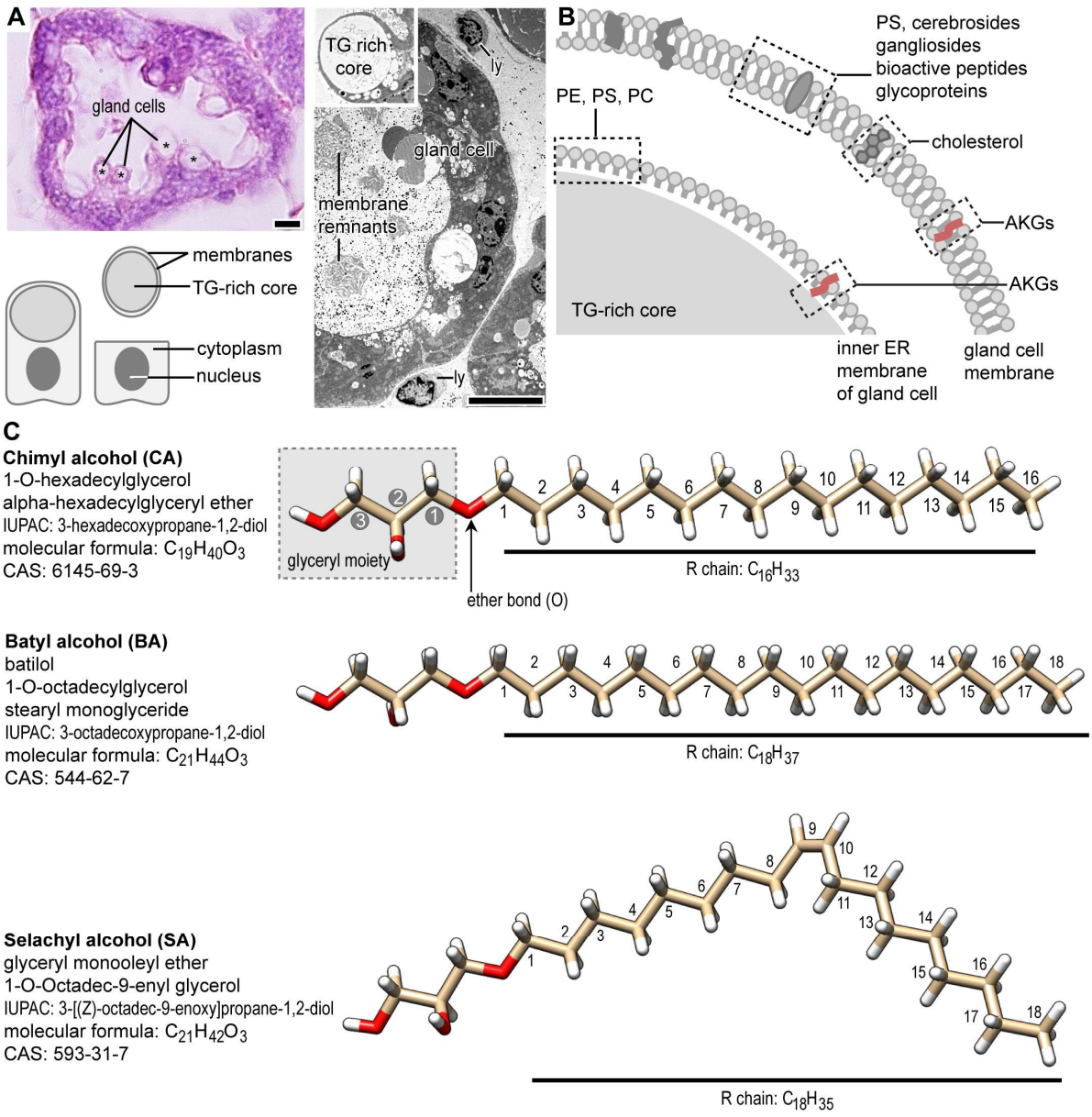

Supplemental Figure 1. Lipid secretion mechanism of the mammary gland and structure of AKGs found in human breast milk

(**A**) *Top left:* section of a mouse mammary gland acinus stained with eosin. Asterisks show lipid droplets before secretion. Scale bar 10 µm. *Top right:* transmission electron microscopy image of a lactating mouse mammary gland. TG: triglyceride, ly: lymphocytes, which are typical antibody secreting cells in the lactating mammary gland (1). Scale bar 10 µm. *Bottom:* schematic illustration of the mechanism of apocrine secretion. (**B**) Structure of a breast milk lipid droplet. Due to the apocrine secretion mechanism, the TG-rich core of the lipid droplet is covered by the single phospholipid layer of the endoplasmic reticule (ER) and the phospholipid bilayer of the cell membrane (2, 3). PS: phosphatidylserine, PE: phosphatidylethanolamine, PC: phosphatidylcholine (**C**) Structure of breast milk AKGs.

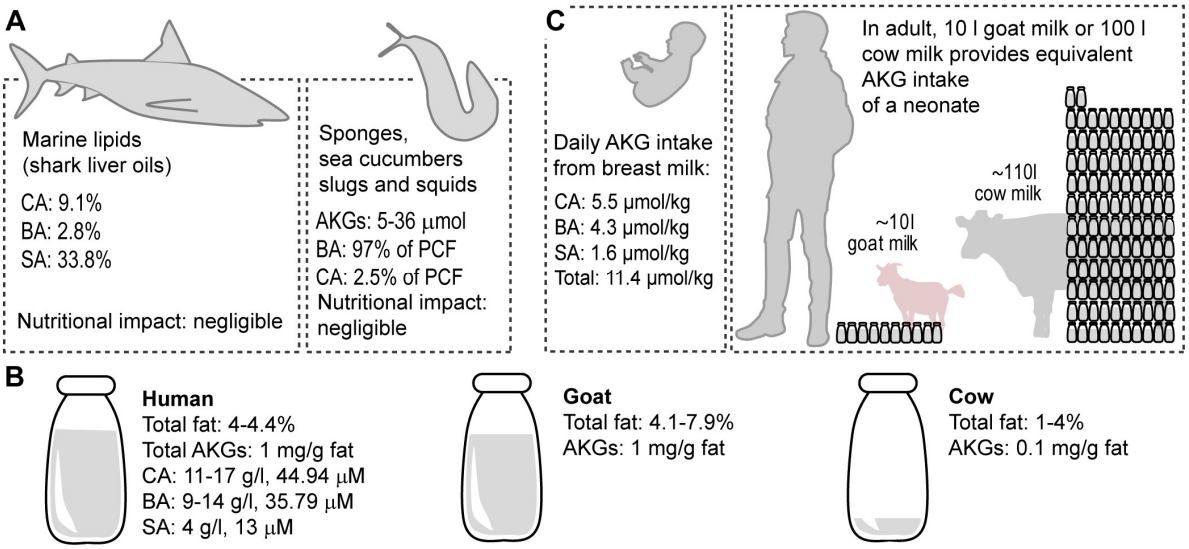

Supplemental Figure 2. Possible sources of AKGs in human nutrition

(**A**) AKGs (chimyl alcohol [CA], batyl alcohol [BA] and selachyl alcohol [SA]) are enriched in so-called marine lipids or "shark liver oils", which are present in the liver of certain shark species (4), the viscera of mollusks, cells of sponges (5), corals (6) and sea cucumbers (7). These sources, however, do not have a nutritional impact. For instance, sponges and slugs are not consumed, and molluscan viscera are removed during food processing. The so-called "shark liver oils" are used in certain folk remedies without proven medical benefits (8). Similarly, little is known on the metabolic effects of AKGs. In diet-induced obesity, an SA-rich diet reduces adiposity (9), although the applied doses are magnitudes higher than the AKG concentrations in tissues. AKGs are synthesized in the ether lipid metabolism (10), although the precise mechanism is unknown. AKG synthesis is characterized only in archaea and bacteria (11), and the enrichment of AKG-like ether lipids is known in marine sediment, from which they potentially enter the food chain (11, 12). PCF: phosphocholine fraction. (**B**) Estimated AKG content of human, goat and cow milk, based on previously published values (13-17). (**C**) Daily AKG intake of a human neonate and its theoretical equivalent in an adult. Of note, a human adult is unlikely to consume the similar amount of AKGs as a neonate. Hence AKGs are lipid species that are taken up in a relevant amount solely by breastfeeding.

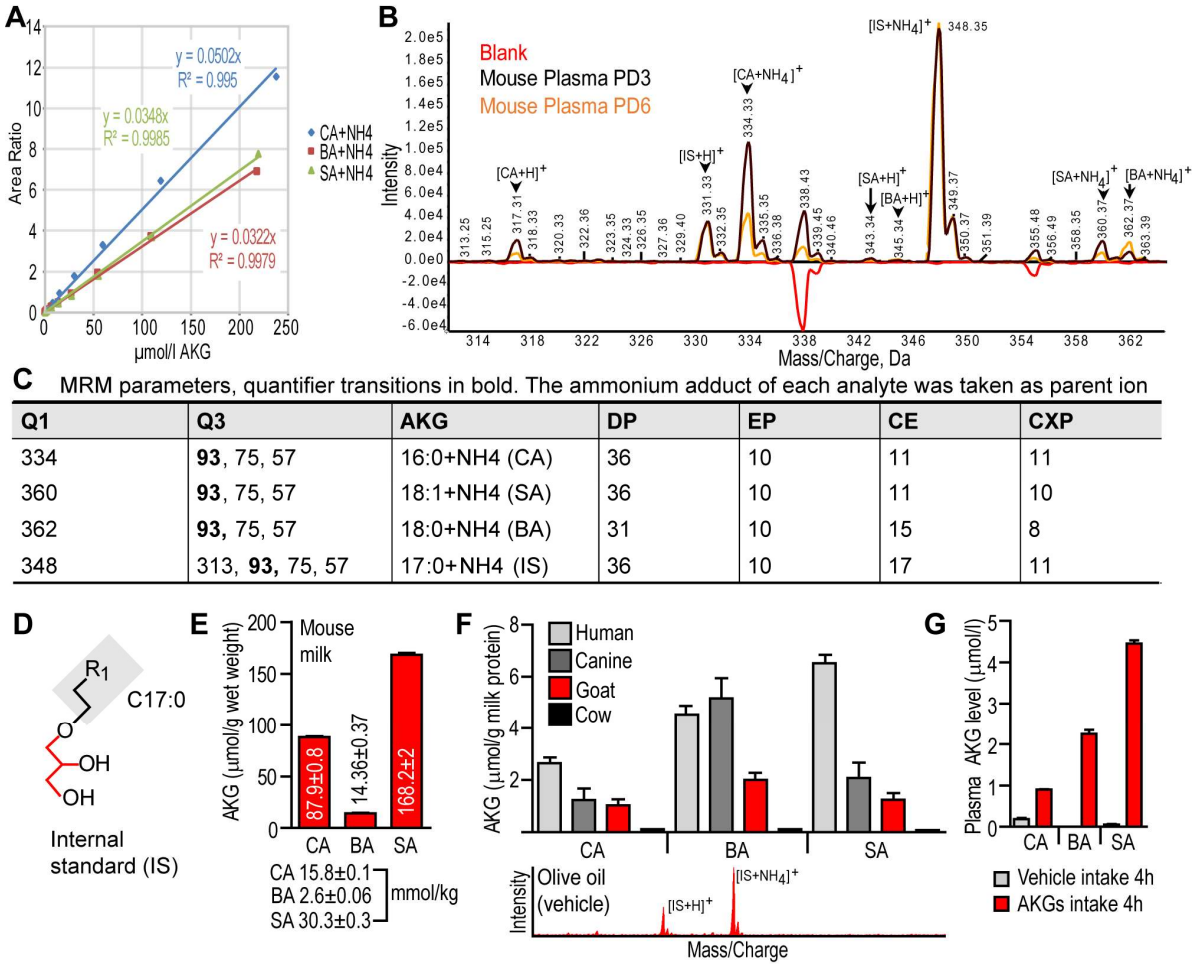

Q1	Q3	AKG	DP	EP	CE	CXP
334	**93**, 75, 57	16:0+NH4 (CA)	36	10	11	11
360	**93**, 75, 57	18:1+NH4 (SA)	36	10	11	10
362	**93,** 75, 57	18:0+NH4 (BA)	31	10	15	8
348	313, **93,** 75, 57	17:0+NH4 (IS)	36	10	17	11

Supplemental Figure 3. Measurement of AKG levels with nano-electrospray ionization tandem mass spectrometry

(**A**) Calibration curve of AKGs and (**B**) a representative mass spectrogram. For better visibility, spectrum of the blank (Milli-Q® water, processed in the same manner as the samples) is mirrored on the X-axis. Precursor ion spectrum of AKGs (CA, BA, SA) in plasma of neonate mice on PD3 and PD6. The spectrum shows the precursor (parent) ions of the characteristic AKG fragment ions. (**C**) Multiple Reaction Monitoring (MRM) parameters. Quantifier transitions highlighted in bold. Q1: quadrupole 1, Q2: quadrupole 2, DP: declustering potential, EP: entrance potential, CE: collision energy, CXP: cell exit potential (**D**) Structure of the internal standard used in the analysis. We used a C17:0 side chain AKG. (**E**) AKG levels in mouse breast milk normalized to net weight *(Top)*; and calculated daily AKG intake of a neonate mouse *(Bottom)*. (**F**) AKG content of human, canine, goat and cow milk. The human sample was collected in the 2nd month of breastfeeding. The canine samples were collected from three lactating dogs. Goat milk was obtained from a commercial source (Allgäu region, Germany). Raw cow milk was obtained from a local farmer in Ulm, Germany. *Bottom:* Olive oil was free from AKGs. Mass spectrogram peaks indicate signal from the internal standard (IS). (**G**) Plasma levels of AKGs in adult mice orally fed with olive oil vehicle (AKG-free) or 0.4 µmol/kg AKGs dissolved in olive oil. Plasma was collected 4 h after ingestion of vehicle or AKGs.

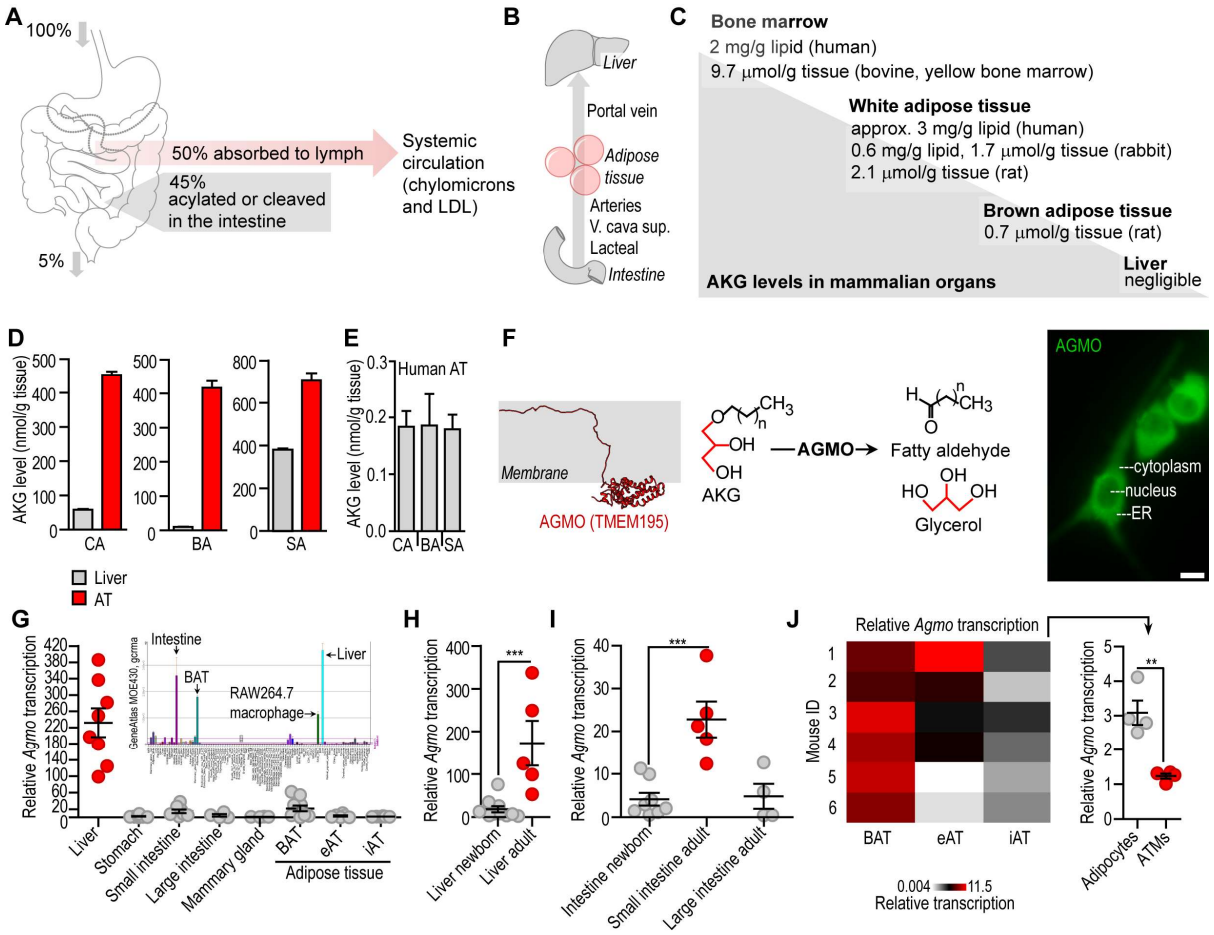

Supplemental Figure 4. Absorption and catabolism of AKGs

(**A**) AKGs are readily absorbed through intestinal epithelia, although approximately one-half of the ingested AKGs are degraded by intestinal epithelial cells. The absorbed AKGs are taken up by the lymphatic vessels of the intestinal villi and are built into chylomicrons and LDL (18). (**B**) Transport route of AKGs in the circulation. Similar to other lipids, AKGs travel through the lymphatic vessels to the superior *vena cava*, where they enter the systemic circulation and reach the adipose tissue. AKGs reach the liver through the portal vein. (**C**) Summary of the literature reporting AKG levels in mammalian tissues (10, 13-17, 19-21). Normalization of the values and the analytical techniques used vary; notably, however, AKGs are present in adipocyte-rich tissues, due to their lipophilic nature. Direct comparison of these data, or their use as reference values, is challenging because of differences in the accuracy of the analytical techniques used. (**D**) AKG levels in mouse liver and adipose tissue (AT) at PD10. (**E**) AKG levels in human adult subcutaneous AT. The samples were collected during abdominoplasty of three patients (female, 27 years-old; males, 39 and 43 years-old). (**F**) *Left:* three-dimensional structure of AGMO created using LOMETS server (22) and scheme of its catalytic activity. AGMO cleaves AKGs and lyso-PAF to release fatty aldehydes and glycerol (23-25). *Right:* immunohistochemistry of AGMO in IL-4-treated (10 ng/ml, 18 h) mouse macrophages. Scale bar 25 µm. (**G**) *Agmo* levels in adult mouse organs. Transcription was normalized to *Bactin*. Insert shows BioGPS map of *Agmo* transcription in mouse. (**H**) *Agmo* transcription in mouse liver at PD10 and PD56. (**I**) Comparison of *Agmo* transcription in mouse intestine at PD10 and PD56. (**J**) Heat map illustrating *Agmo* levels in various AT depots obtained from 6 adult mice (BAT; brown adipose tissue, e/iAT, epididymal/inguinal AT). Comparison of *Agmo* levels in mouse adipocytes and ATMs. We used C57BL/6 male mice for the assays in G–K. ** $p<0.01$, ***$p<0.001$, Student´s 2-tailed unpaired t-test.

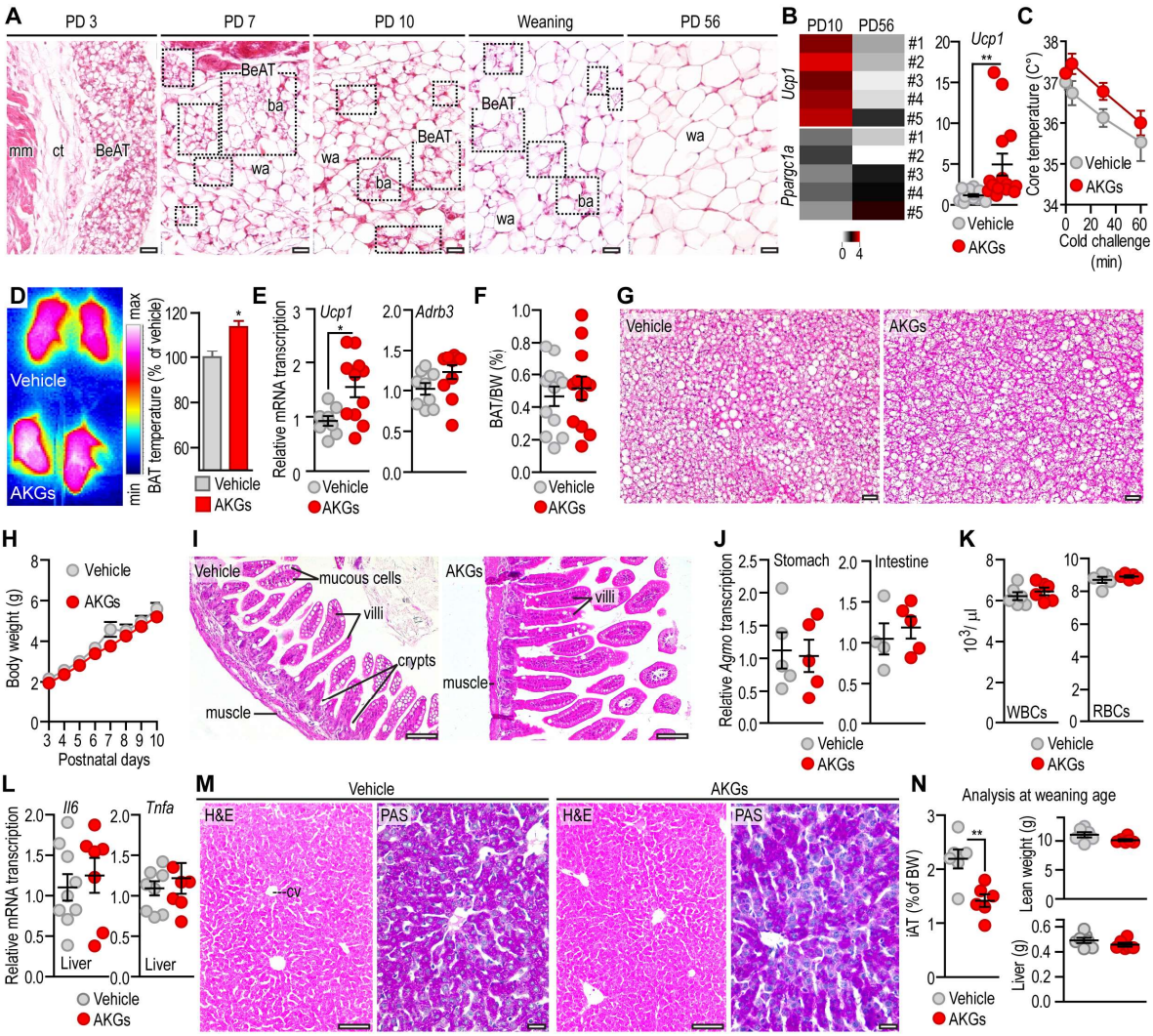

Supplemental Figure 5. Development of BeAT in C57BL/6 mice. Effects of AKG supplementation in neonates

(**A**) Representative hematoxylin and eosin (H&E)-stained sections of the iAT at PD3, PD10, weaning and PD56 in male C57/BL6 mice. BeAT: beige adipose tissue, ct: connective tissue, mm: muscles, wa: white adipocyte, ba: beige adipocyte. Scale bars 50 µm. (**B**) Relative transcription of *Ucp1* and *Ppargc1a* in iAT at PD10 and PD56 in male C57/BL6 mice, n=5. *Right:* Dot plot representation of *Ucp1* values of Figure 1I. (**C-N**) Effects of AKG supplementation in neonate mice. Treatment scheme is shown in Figure 1C. (**C**) Core temperature of vehicle- or AKG-treated mice during cold (10°C) challenge. (**D**) Infrared image of the mice and BAT temperature. (**E**) Relative transcription of BeAT-marker genes in BAT. (**F**) BAT weight. (**G**) BAT histology by H&E staining. Scale bar 50 µm. (**H**) Weight gain across the treatment. (**I**) Histology of the intestine on PD10 by H&E staining. Scale bar 10 µm. (**J**) *Agmo* transcription in stomach and intestine on PD10. We assayed *Agmo* levels to test whether AKG intake induced *Agmo* transcription, which could potentially lead to AKG degradation in the intestinal epithelium. (**K**) Hematology of the vehicle- and AKG-treated mice on PD10. (**L**) Transcription of *Il6* and *Tnfa* in the liver at PD10. (**M**) Histology of liver at PD10 by H&E and periodic acid-Schiff (PAS) staining. cv: central vein, scale bar 50 µm. (**N**) Inguinal AT (iAT) weight of vehicle- and AKG-treated mice at weaning; lean weight remained unaffected by AKG treatment. *p<0.05, **p<0.01 Student´s 2-tailed unpaired t-test

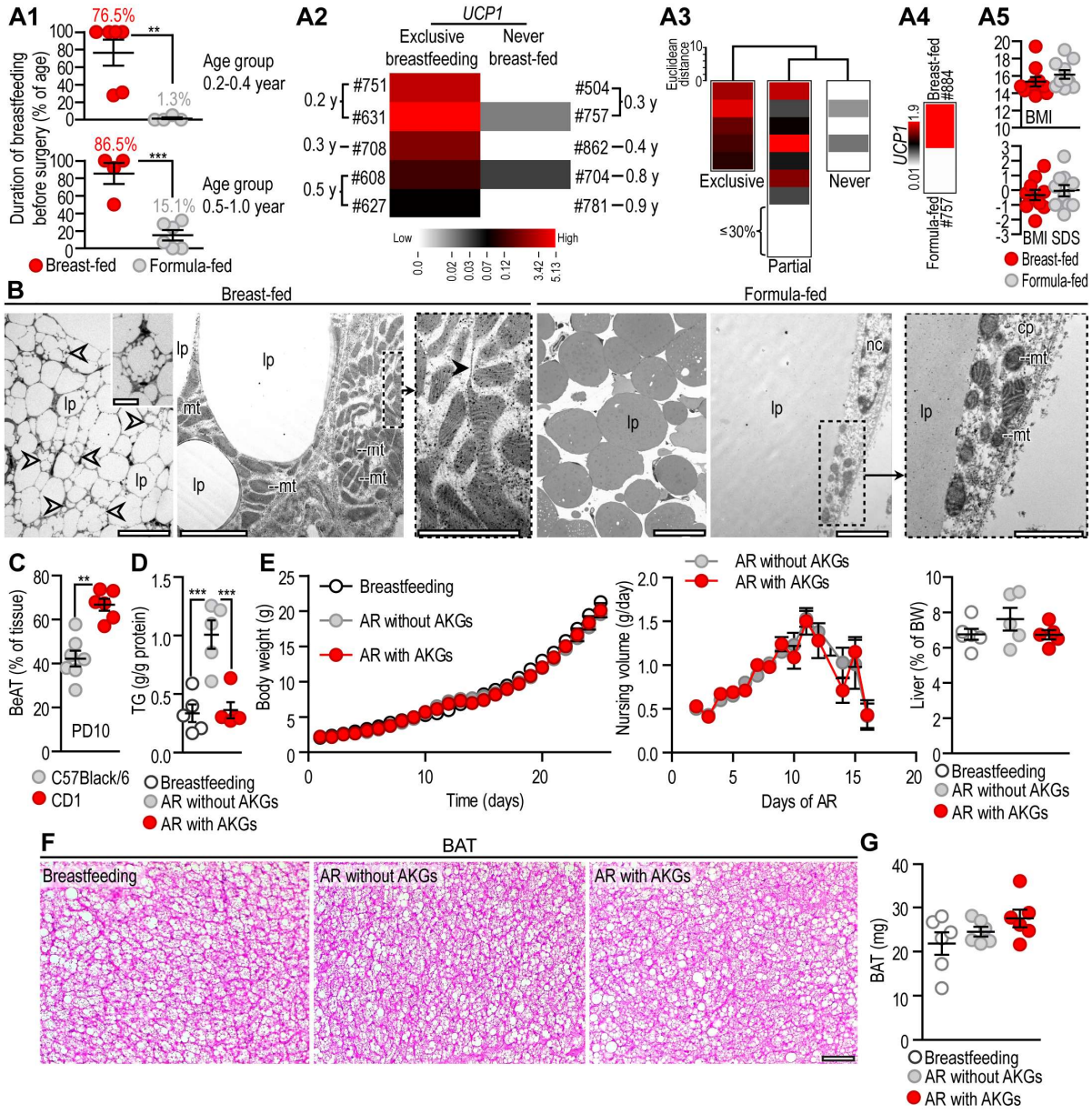

Supplemental Figure 6. *UCP1* transcription and subcellular structure of AT in human infants. Artificial rearing experiment in CD1 neonates

(**A1**) Breastfeeding length of the human infants studied. (**A2**) Relative adipose *UCP1* level in infants exclusively breast-fed and never breast-fed. p=0.0079, Mann-Whitney-U-test (**A3**) Relative adipose *UCP1* transcription of infants clustered in three groups (exclusively breast-fed, partial breast-fed and never breast-fed). (**A4**) Adipose *UCP1* levels in infants of type 2 diabetic mothers. (**A5**) BMI of the studied infants. (**B**) Semi-thin sections and transmission electron microscopy of AT from breast-fed and formula-fed infants. lp: lipid droplet, mt: mitochondria, cp: cytoplasm, nc: nucleus. Clear arrowheads indicate multilocular fat cells, black arrowhead labels mitochondrial fission site. Scale bars from left to right: 25 µm, 2 µm, 1 µm, 25 µm, 2 µm, 1 µm. (**C**) Amount of BeAT in C57BL/6 and CD1 mice at PD10. (**D**) TG content of iAT on day 34 of breast-fed and artificially reared (AR) mice. (**E**) *Left:* Body weight of breast-fed and AR mice, measured daily at 8:00 am. *Middle:* Nursing volume of AR mice. *Right:* Liver weight on day 34 of breast-fed and AR mice. BW: bodyweight (**F,G**) Histology and weight of BAT of breast-fed and AR mice. Scale bar 80 µm. **p<0.01, ***p<0.001 Student´s 2-tailed unpaired t-test (C) and one-way ANOVA with Dunnett´s post-hoc test (D)

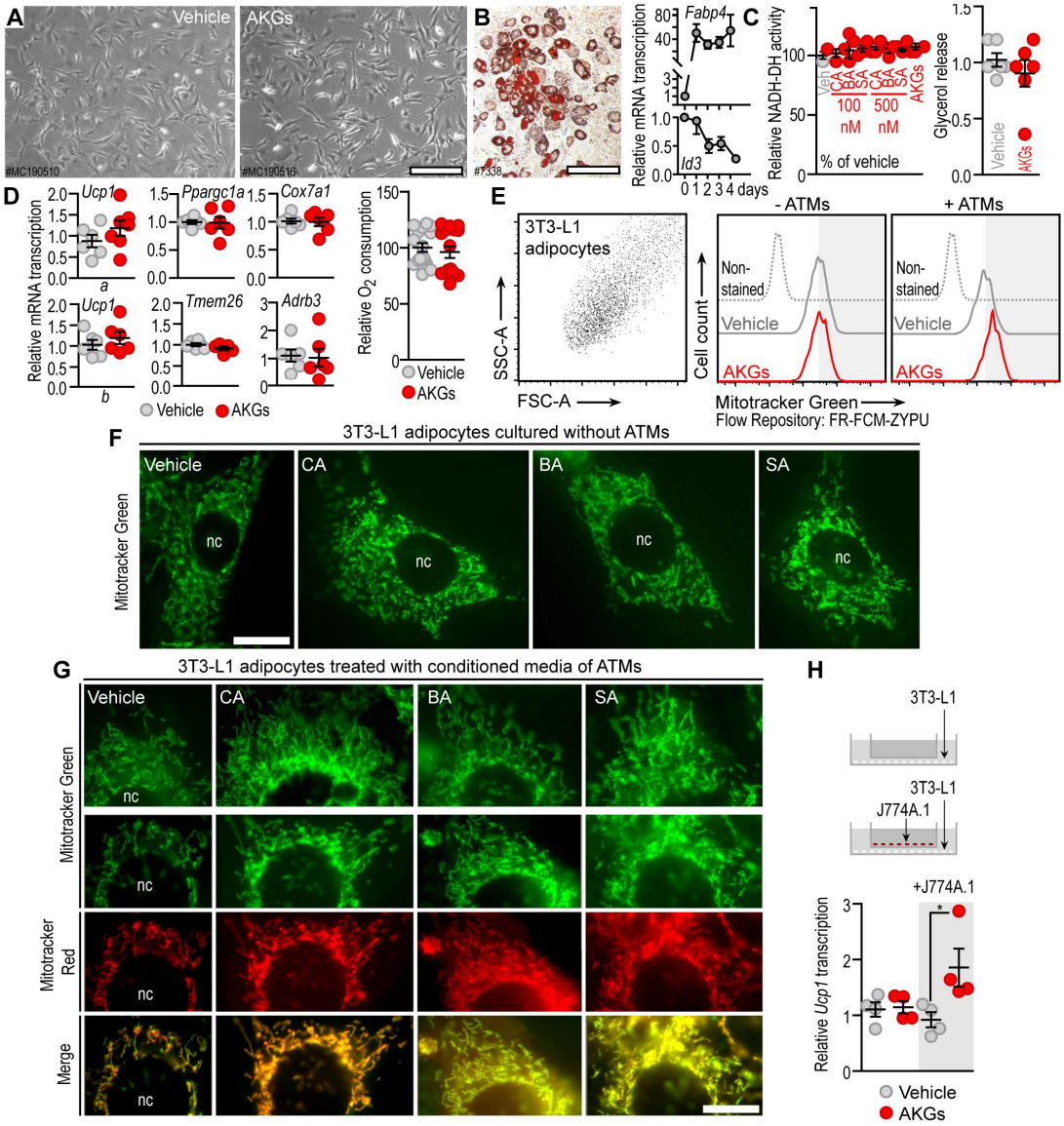

Supplemental Figure 7. Effects of AKGs on adipocytes

(**A**) 3T3-L1 preadipocytes were treated with vehicle or AKGs for 18 h. Scale bar 50 µm. (**B**) 3T3-L1 adipocytes following one week of adipogenic differentiation, stained with oil red-O. Scale bar 50 µm. Transcription of *Fabp4* and *Id3* during adipogenic differentiation. (**C**) NADH-DH activity and glycerol release of AKG-, or vehicle-treated 3T3-L1 adipocytes. (**D**) *Ucp1* transcription in 3T3-L1 preadipocytes (a) and adipocytes (b); and transcription of BeAT genes in 3T3-L1 adipocytes treated with vehicle or AKGs for 18 h. *Right:* O_2 consumption (120 min) following 18 h treatment with vehicle or AKGs. (**E**) FACS analysis of 3T3-L1 adipocytes, cultured without (-ATMs) or with (+ATMs) ATMs using a transwell system. Fluorescence intensity of Mitotracker Green (MTG) was measured following treatment with vehicle or 100 nM AKGs for 4 h. (**F**) Fluorescent microscopy images showing MTG-labeled mitochondria in 3T3-L1 adipocytes. Adipocytes were treated with vehicle or AKGs for 18 h. Scale bar 10 µm. (**G**) Fluorescent microscopy images showing MTG-labeled mitochondria in 3T3-L1 adipocytes *(Top)* and double labeled with MTG and Mitotracker Red *(Bottom)*. The adipocytes were cultured with conditioned media of ATMs treated with vehicle or AKGs. (**H**) Transwell assay using J774A.1 macrophages and 3T3-L1 adipocytes *(Top)*. Transcription of *Ucp1* in 3T3-L1 adipocytes treated with vehicle or 100 nM AKGs for 4 h in the transwell system *(Bottom)*. *p<0.05 Student´s 2-tailed unpaired t-test

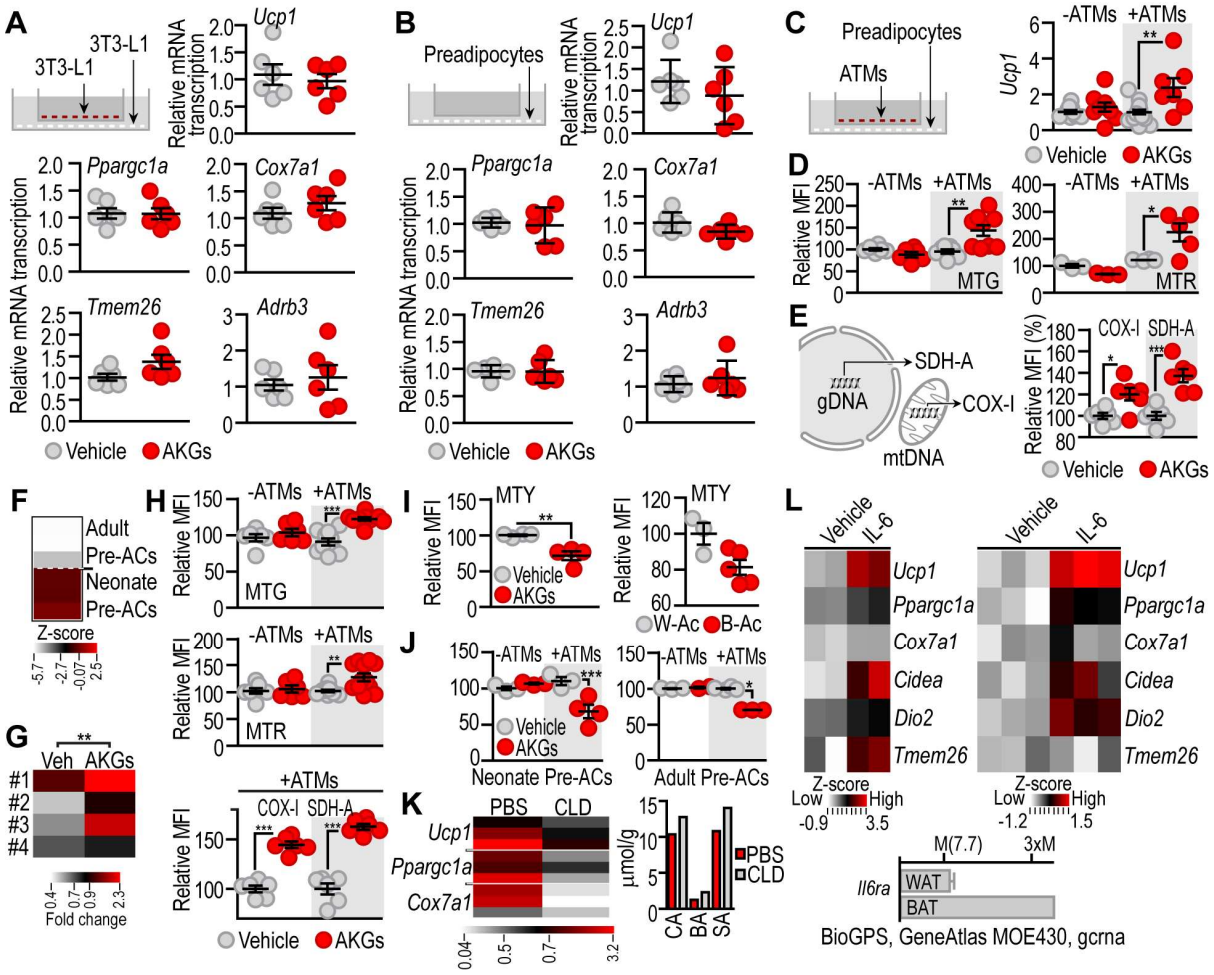

Supplemental Figure 8. Effects of AKGs and IL-6 on preadipocytes and adipocytes

(**A**) 3T3-L1 adipocytes were seeded into a transwell system, and treated with vehicle or AKGs for 18 h. BeAT gene transcription was measured. (**B**) Preadipocytes from adult iAT were treated with vehicle or AKGs for 18 h, and BeAT gene transcription was measured. (**C-D**) Transwell assays using preadipocytes and ATMs from adult mouse iAT. *Ucp1* transcription (C) and relative MFI of Mitotracker Green (MTG) and Mitotracker Red (MTR) (D). (**E**) FACS analysis of mitochondrial biogenesis in adult iAT-preadipocytes, treated for 18 h with conditioned media of AKG-treated adult ATMs. Succinate dehydrogenase complex subunit A (SDH-A) is encoded by genomic DNA (gDNA). Cytochrome c oxidase subunit 1 (COX-I) is encoded by mitochondrial DNA (mtDNA). (**F**) *Ucp1* level in preadipocytes (Pre-ACs) harvested from adult mice, and from six-day-old neonate mouse iAT. (**G**) Preadipocytes of six-day-old neonate mouse iAT were treated with conditioned media of neonate ATMs for 18 h and *Ucp1* transcription was measured. (**H**) Effect of AKGs on neonate mouse preadipocytes after 18 h treatment, without or with the presence of neonate ATMs. (**I**) Mito Thermo Yellow (MTY) signal of adipocytes isolated from vehicle-, or AKG-treated neonate mice on PD10 (see Figure 1C). MTY signal of iAT preadipocytes differentiated into white adipocytes (W-Ac) or induced towards beige differentiation (B-Ac). (**J**) MTY signal in adult or neonate Pre-ACs, treated with vehicle or AKGs for 18 h, without or with the presence of ATMs. (**K**) Mice were injected *i.p.* with PBS-filled liposomes (PBS), or clodronate-filled liposomes (CLD) on postnatal day 3. BeAT gene transcription was measured on postnatal day 7. AKG levels of the ingested breast milk were also measured. (**L**) BeAT gene transcription in 3T3-L1 preadipocytes *(Left)* and adult Pre-ACs *(Right)*. Cells were treated with vehicle or 2 ng/ml IL-6 for 18 h. *Bottom: Il6ra* level in mouse WAT and BAT. *p<0.05, **p<0.001, Student´s 2-tailed, unpaired t-test.

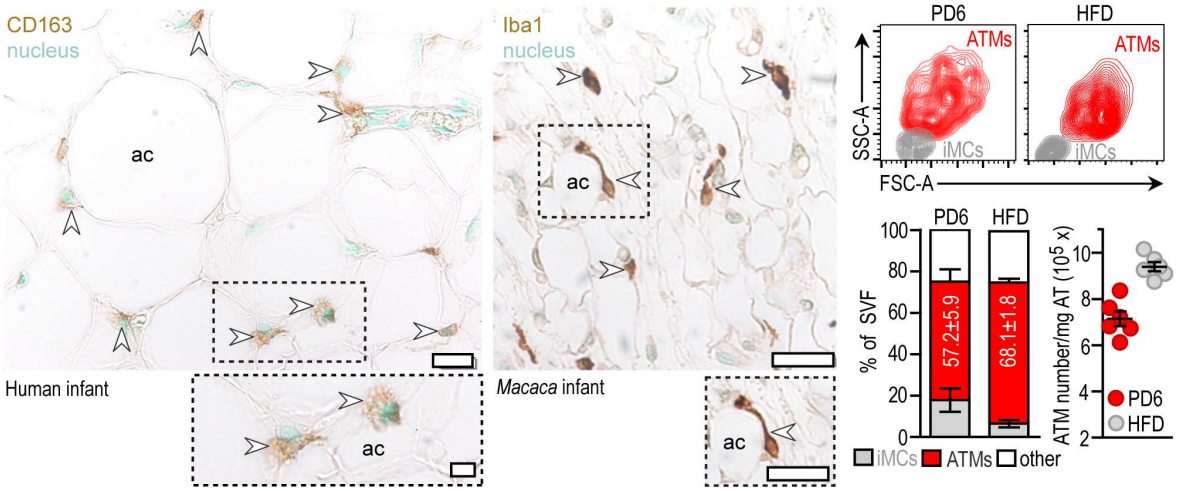

Supplemental Figure 9. **ATMs of the neonate AT**

Left: For better visibility we display here the enlarged Figure 3I. Case numbers of the *Macaca mulatta* infant samples used for Iba1 immunostaining: 2016c331 (4 days old female), 2016c270 (term fetus male stillborn), 2017c349 (14 days old female); protocol approval G005151-R01. *Right:* FACS analysis of stromal vascular fraction isolated from infant mouse iAT on postnatal day 6 (PD6), and iAT of HFD-fed adult C57BL/6 mice. Cells were pooled from 8-11 neonate mice for each data point. ATMs: cell population rich in ATMs, iMCs: cell population rich in immature myeloid cells. These cell populations have previously been characterized by FACS and transmission electron microscopy (26, 27).

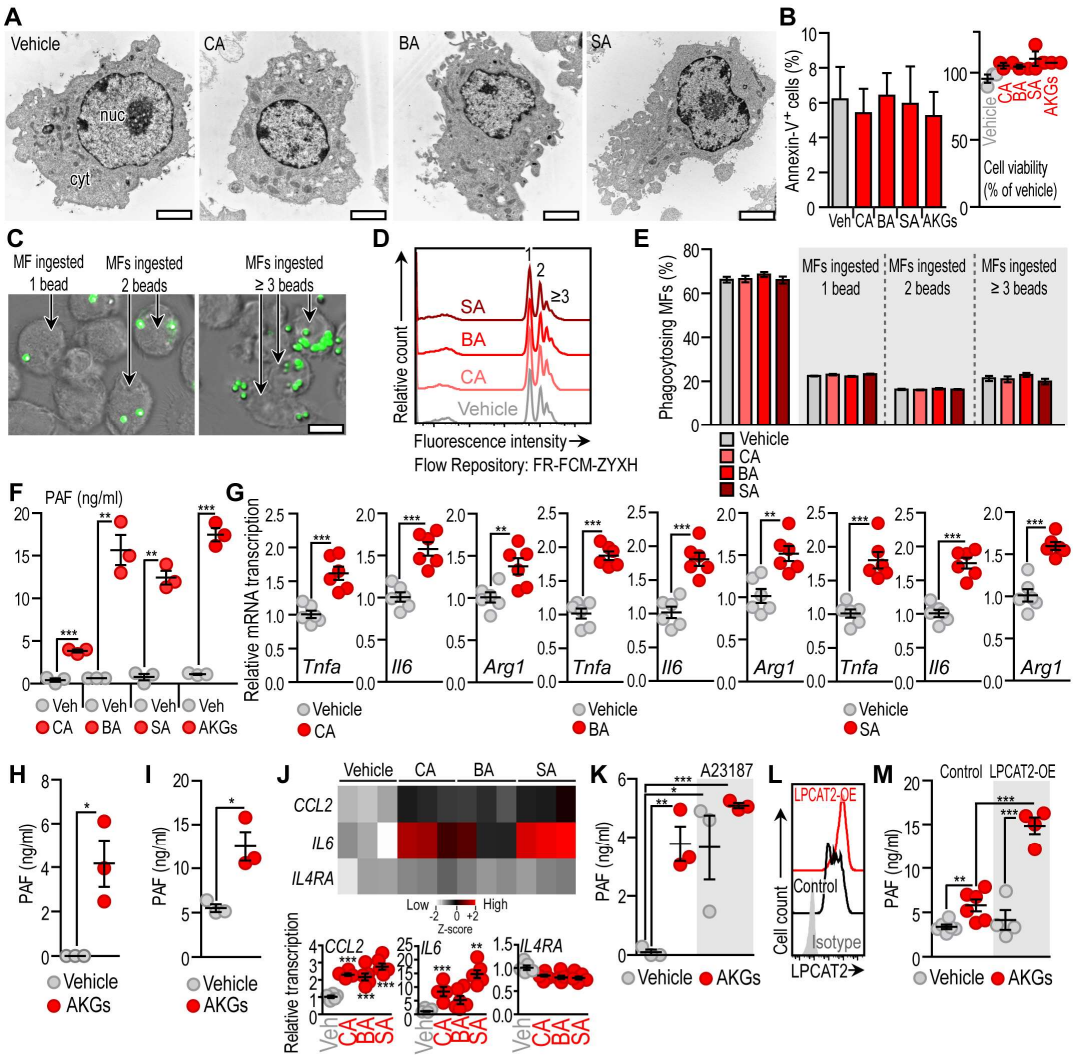

Supplemental Figure 10. Effects of AKGs on macrophages

(**A**) Transmission electron microscopy of macrophages treated with vehicle or AKGs for 18 h. nuc: nucleus, cyt: cytoplasm. Scale bar 2 µm (**B**) Annexin-V labeling and viability of macrophages, treated with 100 nM CA, BA or SA, or their equimolar combination (AKGs) for 18 h. (**C–E**) Phagocytosis activity of 100 nM AKG-treated macrophages. (**C**) Fluorescent microscopy showing macrophages (MFs) with ingested fluorescent latex beads. Scale bar 10 µm. (**D**) FACS analysis of phagocytosis activity after vehicle-, or AKG-treatment. *Peak 1* denotes the fluorescent signal derived from macrophages with one engulfed fluorescent bead; *Peak 2* indicates macrophages with two beads ingested; *Peak ≥3* indicates macrophages with three or more phagocytosed beads. (**E**) Quantification of the percentage of phagocytosing MFs. (**F**) PAF release from J774A.1 cells treated with vehicle (Veh) or 100 nM AKGs for 30 min. Further assays are shown in Figure 4J, Supplemental Figure 10K,M. (**G**) Transcript levels of *Tnfa*, *Il6* and *Arg1* in J774A.1 macrophages treated with 100 nM AKGs for 18 h. (**H**) PAF release from human ATMs treated with AKGs for 30 min. (**I**) THP-1 macrophages have been proven to synthesize PAF from AKGs (28). Treating THP-1 macrophages with AKGs evoked PAF release in 30 min. (**J**) AKG treatment (18 h) evoked PAF-mimicking transcriptional changes in THP-1 macrophages. (**K**) The calcium ionophore A23187 was used to induce PAF release from J774A.1 macrophages. Cells were treated for 15 min. (**L**) FACS analysis of LPCAT2-overexpressing (OE) macrophages. (**M**) PAF release from control, and LPCAT2-OE macrophages. *p<0.05, **p<0.0, ***p<0.001 Student´s 2-tailed unpaired t-test (F-I), one-way ANOVA (K,M).

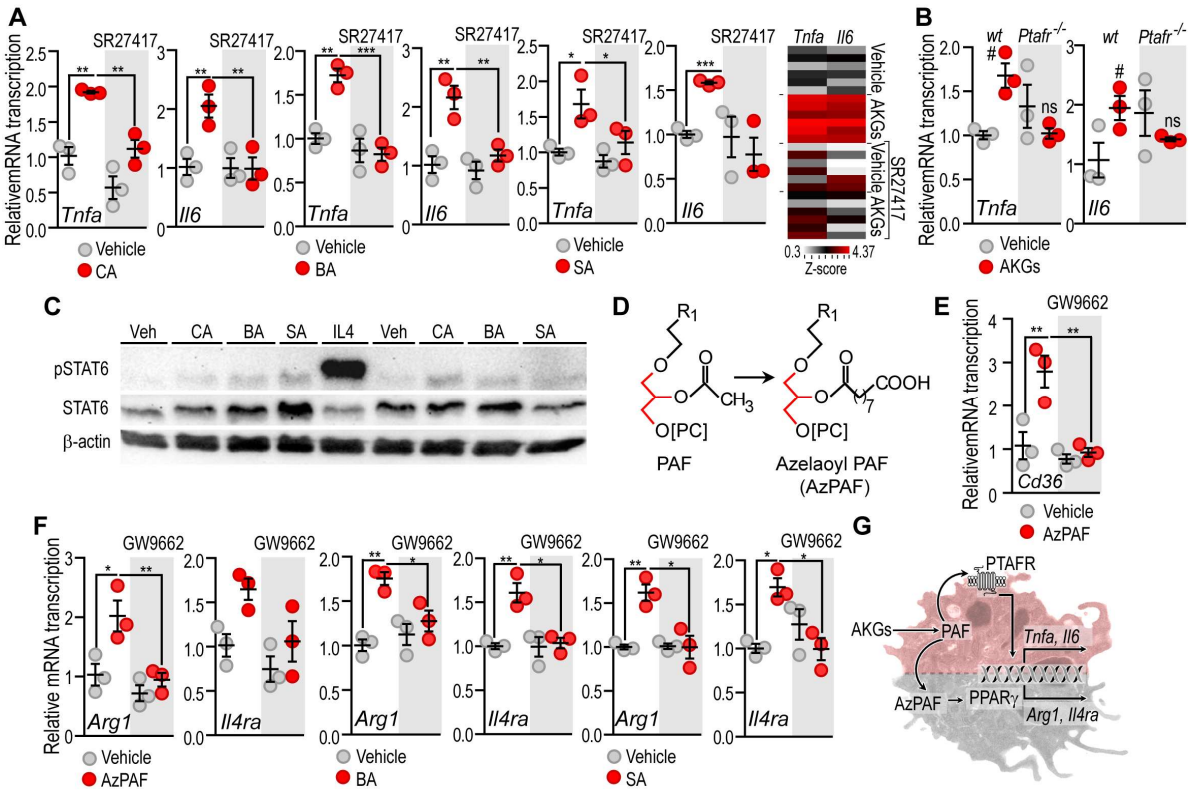

Supplemental Figure 11. Effects of AKGs on macrophages

(**A**) Transcript levels of *Tnfa*, *Il6* and *Arg1* in macrophages treated with 100 nM AKGs for 18 h. We used SR27417 as a platelet-activating factor receptor (PTAFR) blocker. (**B**) Transcript levels of *Tnfa* and *Il6* in wild-type *(wt)* PTAFR-deficient *(Ptafr$^{-/-}$)* macrophages treated with AKGs for 18 h. We used *in vitro* differentiated bone marrow-derived macrophages for this assay. (**C**) Western blot of phosphorylated (p) STAT6 and total STAT6 in J774A.1 macrophages treated with 100 nM AKGs or 100 ng/ml IL-4 for 30 min. (**D**) Scheme of the non-enzymatic conversion of PAF into AzPAF. (**E**) Effect of AzPAF on transcription of the PPARγ target *Cd36*. One set of treatments was carried out in the presence of the PPARγ inhibitor GW9662. (**F**) Effect of AzPAF and the AKGs on the transcription of *Arg1* and *Il4ra* in J774A.1 macrophages. One set of treatments was carried out in the presence of the PPARγ inhibitor GW9662. *p<0.05, **p<0.01 Student´s 2-tailed unpaired t-test #p<0.05, one-way ANOVA with Dunnett´s post hoc test (**G**) Scheme of the effect of AKGs on *Tnfa*, *Il6*, *Arg1* and *Il4ra* transcription. AKGs increase PAF release from macrophages, which in turn increases *Tnfa* and *Il6* transcription. Non-enzymatic conversion of PAF into AzPAF provides ligand for PPARγ, which ultimately triggers *Arg1* and *Il4ra* transcription. Inhibiting PTAFR (panels A and B) or PPARγ (panel F) abolishes the effect of AKGs. Further assays on the effect of AKGs on *Il4ra* and *Arg1* transcription are shown in Figure 4D and Supplemental Figure 10G,J,

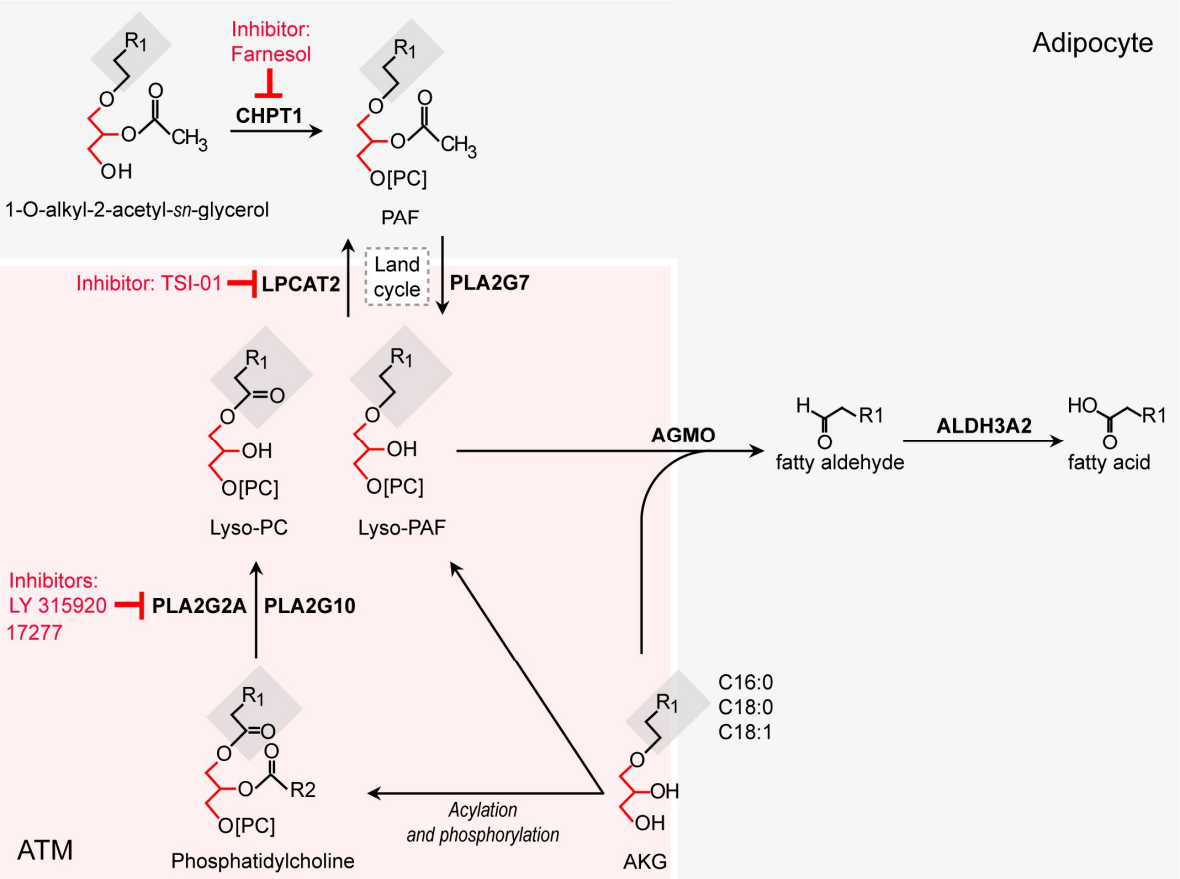

Supplemental Figure 12. Biosynthesis of PAF by ATMs and adipocytes
AKG metabolism by adipocytes and ATMs. CHPT1 synthesizes PAF from 1-O-alkyl-2-acetyl-*sn*-glycerol in the so-called *de novo* PAF synthesis (24, 29). AGMO is an AKG catabolizing enzyme (23). Fatty aldehydes, products of AGMO, are further converted to fatty acids by ALDHA32 (24). LPCAT synthesizes PAF from lyso-PAF and lyso-phosphatidylcholine (lyso-PC) in the so-called remodeling PAF synthesis (23, 29). PLA2G2A and PLA2G10 generate lyso-PC, hence can indirectly fuel PAF synthesis (30-32). PLA2G7 degrades PAF into lyso-PAF. The PAF/lyso-PAF/PAF conversion is called Land´s cycle. AKGs are structurally similar to 1-O-alkyl-2-acetyl-*sn*-glycerol and lyso-PAF, and thus can potentially enter both the *de novo* and the remodeling pathway of PAF synthesis (4, 28). AKGs can also be acylated and phosphorylated (24, 33), and hence serve as substrates for PLA2G2A and PLA2G10. PC: phosphocholine

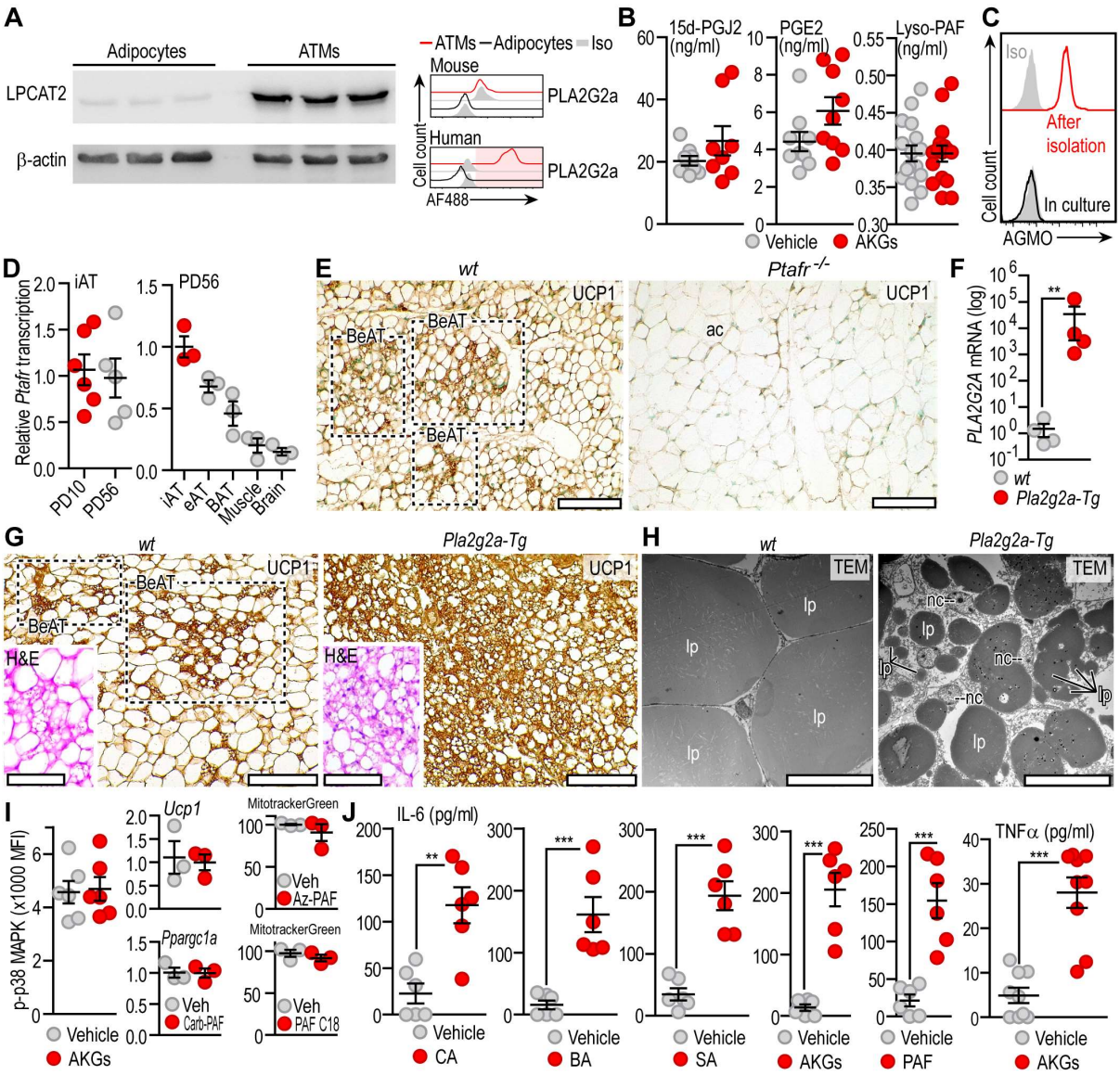

Supplemental Figure 13. Metabolites generated by macrophages in response to AKGs

(**A**) Western blotting of LPCAT2 in mouse ATMs and adipocytes *(Left)*. FACS analysis of PLA2G2a in mouse and human ATMs and adipocytes *(Right)*. (**B**) Metabolites secreted by ATMs treated with AKGs for 30 min. (**C**) FACS analysis of mouse ATMs immediately after their isolation, and after *in vitro* culture for 18 h. (**D**) Expression of *Ptafr* in iAT of C57BL/6 mice at PD10 and PD56 *(Left)*. Expression of *Ptafr* in various organs of adult C57BL/6 mice *(Right)*. (**E**) UCP1 immunostaining of iAT in *wt* and *Ptafr*$^{-/-}$ mice at PD10. Scale bar 80 µm. The *Ptafr*$^{-/-}$ mouse is prone to obesity (34). (**F**) Transcript level of *PLA2G2A* in *wt* and *Pla2g2a-Tg* iAT. (**G**) UCP1 immunostaining of iAT in *wt* and *Pla2g2a-Tg* mice at PD10. *Inserts:* H&E stained sections showing clusters of multilocular fat cells. Also see Figure 5B. Scale bar 80 µm. The *Pla2g2a-Tg* mouse has reduced adiposity, and increased thermogenesis (35). (**H**) Transmission electron microscopy of iAT of *wt* and *Pla2g2a-Tg* mice. lp: lipid vesicle, nc: nucleus. Scale bar 20 µm. (**I**) *Left:* 3T3-L1 adipocytes were incubated for 30 min with conditioned media of ATMs previously treated with vehicle or AKGs for 4 h. FACS analysis of phosphorylated (p)-p38 MAPK. *Middle: Ucp1* and *Ppargc1a* mRNA was measured in 3T3-L1 adipocytes, treated with vehicle or 200 nM carbamyl-PAF (Carb-PAF) for 18h. *Right:* Mitotracker Green signal in 3T3-L1 adipocytes treated with vehicle, 50 nM Az-PAF or 50 nM PAF18:0 for 18h. (**J**) IL-6 and TNFα secreted by ATMs treated with vehicle or AKGs for 4h. *p<0.05, **p<0.01, ***p<0.001 unpaired 2-tailed Student´s t-test

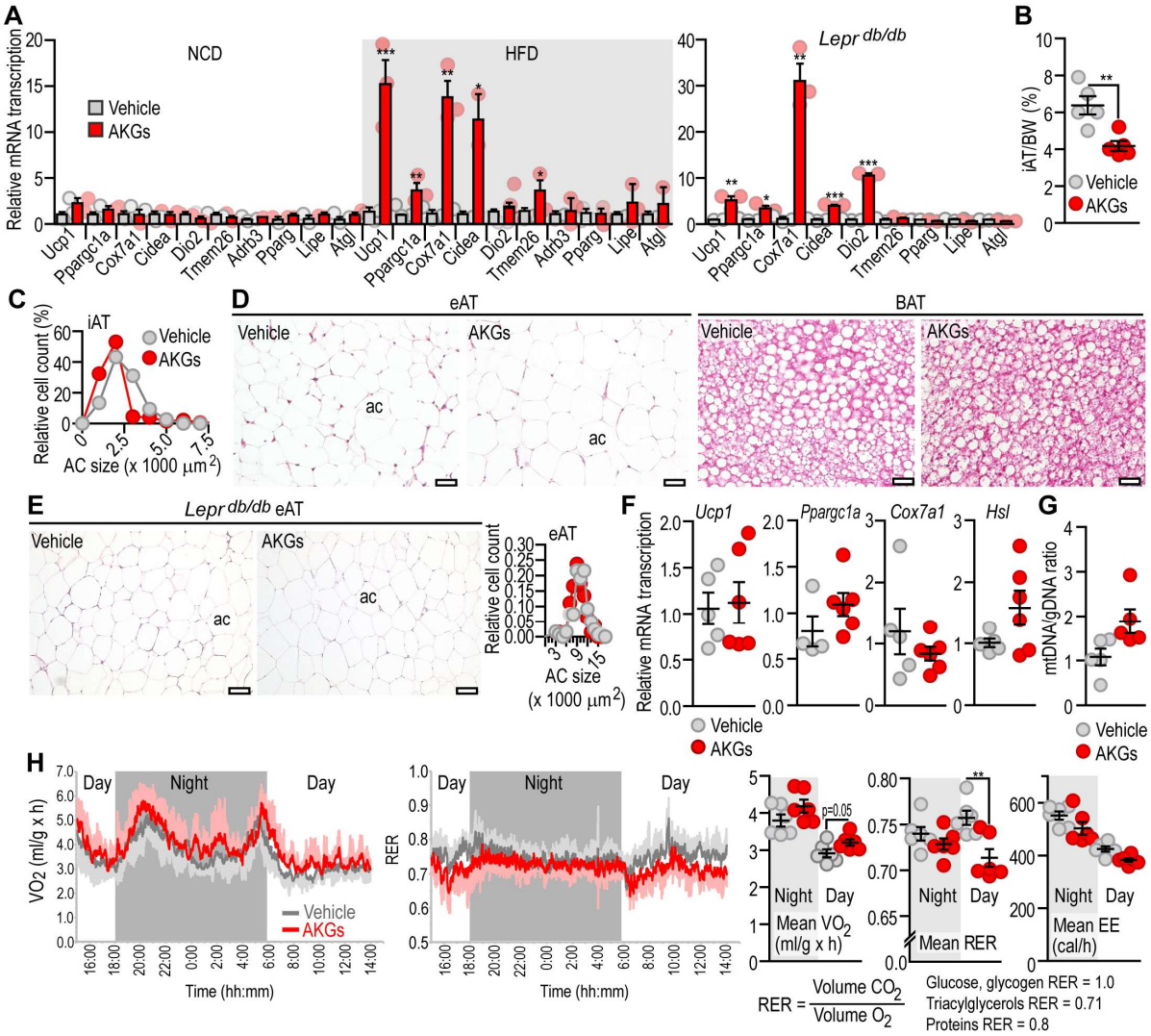

Supplemental Figure 14. Effects of AKGs in adult mice

(**A**) qPCR analyses shown in CIMs of Figure 6A and C. (**B**) Inguinal AT (iAT) weight in HFD-fed mice, treated with vehicle or AKGs. Food intake was not affected by the treatment (2.86±0.19 g/day in vehicle-, and 2.91±0.47 g/day in AKG-treated mice). (**C**) Adipocyte size in iAT of vehicle-, or AKG-treated HFD-fed mice. (**D**) Histology of epididymal AT (eAT) and brown adipose tissue (BAT) in HFD-fed mice treated with vehicle or AKGs. ac: adipocyte, scale bar 50 µm. (**E**) Histology of eAT in *Lepr*$^{db/db}$ mice treated with vehicle or AKGs. Food intake was not affected by the treatment. (**F**) Transcription of BeAT-marker genes in eAT of *Lepr*$^{db/db}$ mice treated with vehicle or AKGs. (**G**) Ratio of mitochondrial DNA (mtDNA) and genomic DNA (gDNA) in iAT of *Lepr*$^{db/db}$ mice treated with vehicle or AKGs. Ratio of mtDNA and gDNA was determined as described (36). (**H**) Indirect calorimetry of HFD-fed obese mice following vehicle-, or AKG-treatment. RER: respiratory exchange rate, EE: energy expenditure; RER is dependent on metabolite supply, as shown by examples of glucose/glycogen, lipids and proteins. *p<0.01, **p<0.01, unpaired 2-tailed Student´s t-test

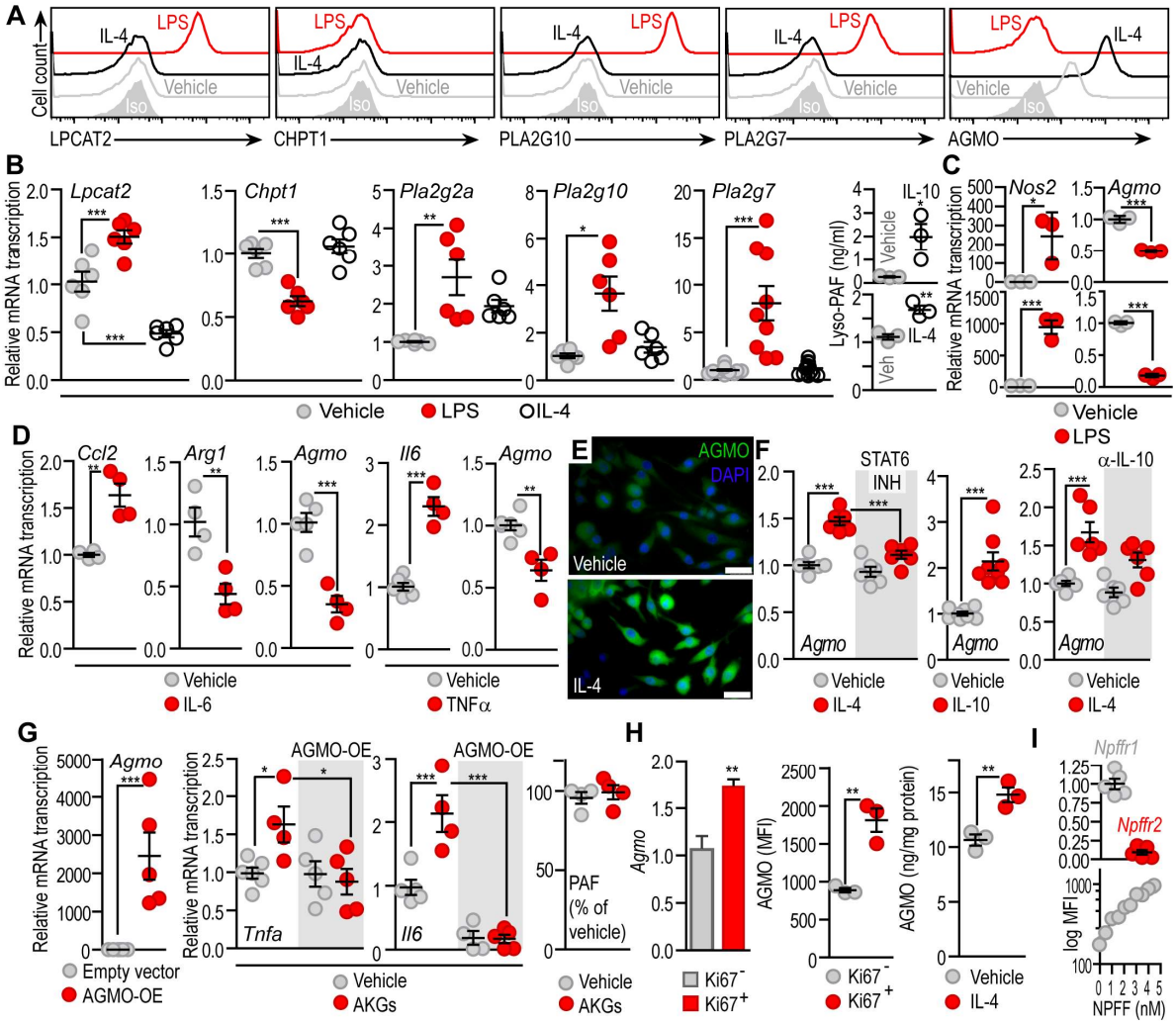

Supplementary Figure 15. Regulation of AGMO expression in macrophages

(**A**) FACS analysis of enzymes involved in PAF metabolism in mouse ATMs. Effect of lipopolysaccharide (LPS) and IL-4. (**B**) Effect of LPS and IL-4 on the transcription of genes involved in PAF metabolism in J774A.1 macrophages; and the effect of IL-4 and IL-10 on lyso-PAF synthesis of ATMs *in vitro*. Cells were treated for 18h with LPS, IL-4 or IL-10 as described before (26). (**C-D**) Effect of IL-6, TNFα and LPS on *Agmo* transcription in J774A.1 macrophages. As positive controls, marker genes of macrophage polarization (*Ccl2, Arg1, Il6, Nos2*) were also assayed. (**E**) Fluorescent microscopy images of vehicle-, or IL-4 (10 ng/ml, 18 h)-treated J774A.1 macrophages. Scale bar 25 μm. (**F**) Transcription of *Agmo* in IL-4 and IL-10 treated macrophages. STAT6-INH: STAT-6 signaling was inhibited with 200 nM AS1517499 as described before (26). α-IL-10: IL-10 was neutralized with an IL-10 blocking antibody. (**G**) Mouse *Agmo* cDNA was overexpressed in J774A.1 macrophages. Level of *Agmo* mRNA was measured 24 h after transfection. Cells transfected with an empty vector served as controls. Control or AGMO-overexpressing (AGMO-OE) macrophages were treated with AKGs for 18 h and *Tnfa* and *Il6* mRNA levels and PAF secretion were measured. (**H**) Transcript level of *Agmo* in Ki67$^-$ and Ki67$^+$ ATMs. Expression of AGMO in Ki67$^-$ and Ki67$^+$ J774A.1 macrophages measured by FACS. AGMO protein level in ATMs treated with vehicle or 10 ng/ml IL-4 for 4 h, measured with ELISA. (**I**) Ratio of *Npffr1* and *Npffr2* in adipocytes, and binding of NPFF to 3T3-L1 adipocytes (26). *p<0.05, **p<0.01, ***p<0.001 (t-test or one-way ANOVA) Further FACS analyses are shown in Flow Repository FR-FCM-ZY7H and ZY9E.

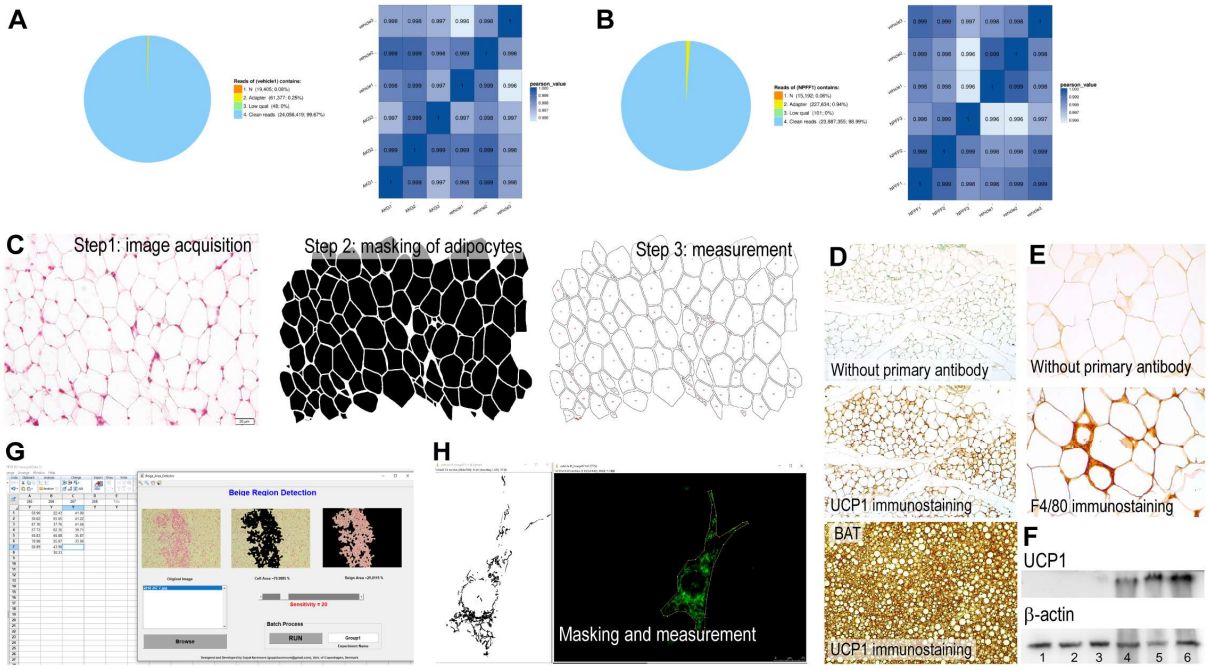

Supplemental Figure 16. Supporting information for NGS and image analysis

(**A**) Percentage of clean reads and correlation matrix of samples used for NGS (ATMs treated with vehicle or AKGs, shown in Figure 4A, 6H, source files are accessible in GEO (GSE125405). (**B**) Percentage of clean reads and correlation matrix of samples used or NGS (adipocytes treated with vehicle or NPFF, shown in Figure 7E, source files are accessible in GEO (GSE125405). (**C**) Adipocyte size was measured with ImageJ software (NIH). Images were masked to label the borders of each adipocyte, and area measurement was carried out using built-in script of ImageJ. (**D-E**) Controls of UCP1 and F4/80 immunostaining. (**F**) Western blot of UCP1 in AT samples on PD56. 1-3 iAT, 4-6 BAT. (**G**) BeAT area was measured with in-house software, which upon publication is available for use. Briefly, the software was adjusted to recognize BeAT morphology cell clusters using H&E–stained sections. Total tissue area and percentage of BeAT area is calculated automatically. As a validation, we used ImageJ-analyzed samples as a comparison. (**H**) Mitochondrial content was measured using ImageJ with the publicly available Mitophagy Macro script, developed by Ruben K. Dagda, according to the application´s instructions (37). To avoid mitochondrial swelling to be misidentified as increased mitochondrial content, we calculated the ratio of area/perimeter and normalized it to minor axis of mitochondria. This value remained constant across experimental groups.

Supplemental Table 1. Plasma AKG levels in infant C57BL/6 mice

	CA (μmol/g protein)	BA(μmol/g protein)	SA(μmol/g protein)
PD3	0.706±0.253	0.294±0.052	0.406±0.147
PD6	0.791±0.265	0.292±0.065	0.354±0.051

Values are from five litters of mice on postnatal day (PD) 3 and 6. Plasma samples were pooled in each litter, due to the small blood volume of infant mice. Each litter consisted from 8-9 infant mice. AKG levels were determined with nano-electrospray ionization tandem MS.

Supplemental Table 2. Part A. Supplementary data on the infants involved in the study

ID	Sex*	Age in year	Height SDS	BMI SDS	Gestational age in weeks	Preterm birth 0=no 1=yes	Current breastfeeding **	Exclusive breastfeeding **	Ever breastfed **	Months of breastfeeding ***
751	1	0.2	-1.51	-0.11	38	0	1	1	1	
631	1	0.2	1.19	-0.21	35	1	1	1	1	
708	1	0.3	1.30	0.90	36	1	1	1	1	
504	1	0.3	0.42	-0.39	38	0	0	0		
884	1	0.3	0.80	0.30	28	1	1	0	1	
757	1	0.3	-0.77	2.30	32	1	0	0	0	
649	1	0.3	-0.10	-1.15	40	0	0	0	1	1
553	0	0.4	-0.60	0.86	36	1	0	0	1	0.3
650	0	0.4	-0.07	-1.07	36	1	0	0	1	1.5
862	1	0.4	0.23	0.27	37	0	0	0	0	
608	1	0.5	-0.36	-2.09	31	1	1	0	1	
557	0	0.5	-0.40	-1.00	39	0	0	0	1	2
627	1	0.5	-1.40	-0.6	30	1	1	1	1	
831	1	0.6	1.34	-1.65	39	0	0	0	1	0.5
655	1	0.7	-0.97	0.47	34	1	0	0	1	2
704	1	0.8	1.21	-0.99	37	0	0	0		
781	1	0.9	0.66	-1.01	34	1	0	0	0	
654	1	0.9	0.0	0.8	40	0	0	0	1	3
634	1	1.0	0.06	-0.89	40	0	0	0	1	11
740	1	1.0	0.34	1.66	40	0	0	0	1	6

*1: male, 0: female

** 1: yes, 0: no

***: applicable only if there was not current breastfeeding

Height SDS: height standard deviation score, BMI SDS: body mass index standard deviation score. Both scores are used to evaluate infant/child growth and weight gain (38, 39). The standard deviation score (SDS) reflects to the deviation of an individual´s value from the median value of a reference population, divided by the standard deviation of the reference population (40-43).

Supplemental Table 2. Part B. Supplementary data on the infants involved in the study

ID	Mother's age at birth in years	Type of elective surgery	Length (cm)	Weight (kg)	BMI	Mother's weight at surgery (kg)	Mother's height at surgery (cm)	Mother´s BMI at surgery	Diabetes state of mother
751	37.4	herniotomy	75	8.4	14.9	61	180	18.8	non-diabetic
631	29.4	herniotomy	60	5.4	15.0	83	163	31.2	non-diabetic
708	19.0	herniotomy	61.8	6.44	16.9	62	161	23.9	n/a
504	29.0	herniotomy	61	5.7	15.3	50	167	17.9	non-diabetic
884	31.7	herniotomy	55	4.24	14.0	61	165	22.4	type 2
757	31.9	herniotomy	55.7	5.9	19.0	110	165	40.4	type 2
649	24.3	herniotomy	63.3	5.95	14.8	65	165	23.9	non-diabetic
553	22.3	herniotomy	58.5	5.715	16.7	65	160	25.4	non-diabetic
650	22.4	herniotomy	60.7	5.27	14.3	65	163	24.5	not avalable
862	32.7	herniotomy	65	7.1	16.8	91	165	33.4	non-diabetic
608	42.3	herniotomy	62	5.265	13.7	52	162	19.8	non-diabetic
557	36.0	herniotomy	65	6.3	14.9	60	160	23.4	non-diabetic
627	29.9	herniotomy	59	5.36	15.4	65	160	25.4	non-diabetic
831	19.8	orchidopexy	74.5	8.2	14.8	100	176	32.3	non-diabetic
655	35.0	herniotomy	66	7.59	17.4	60	160	23.4	non-diabetic
704	30.7	herniotomy	76	9	15.6	60	160	23.4	non-diabetic
781	26.2	herniotomy	75	8.75	15.6	n/a	n/a	n/a	non-diabetic
654	24.9	orchidopexy	75	10.1	18.0	60	168	21.3	non-diabetic
634	32.0	orchidopexy	122	22	14.8	68	174	22.5	non-diabetic
740	33.8	orchidopexy	78	11.8	19.4	80	168	28.3	non-diabetic

None of the mothers developed gestational diabetes during pregnancy. Mothers of infants 884 and 757 had diagnosed and hence treated, type 2 diabetes. *UCP1* levels of infants 884 and 757 are compared in Supplemental Figure 6A. None of the infants had metabolic disease at the time of surgery.

Supplemental Table 2. Part C. Supplementary data on the infants involved in the study

Breast-fed infants		**Formula-fed infants**	
ID	***UCP1* Ct value**	**ID**	***UCP1* Ct value**
751	27.10	504	>40
631	27.93	757	37.87
708	37.50	553	30.40
884	30.47	862	>40
649	21.10	557	35.57
650	36.51	831	>40
608	31.39	655	>40
627	33.71	704	34.21
634	34.67	781	>40
740	29.53	654	>40

Supplemental Table 3.
qPCR primer sequences used in this study (m: mouse, h: human)

m-Bactin	Fw.	GCACCAGGGTGTGATGGTG
	Rev.	CCAGATCTTCTCCATGTCGTCC
m-Gapdh	Fw.	TGACGTGCCGCCTGGAGAAA
	Rev.	AGTGTAGCCCAAGATGCCCTTCAG
m-Ucp1	Fw.	CCTGCCTCTCTCGGAAACAA
	Rev.	CTGTAGGCTGCCCAATGAAC
m-Ppargc1a	Fw.	GACTCAGTGTCACCACCGAAA
	Rev.	TGAACGAGAGCGCATCCTT
m-Cox7a1	Fw.	ATGAGGGCCCTACGGGTCTC
	Rev.	CATTGTCGGCCTGGAAGAG
m-Cidea	Fw.	TACTACCCGGTGTCCATTTCT
	Rev.	ATCACAACTGGCCTGGTTACG
m-Dio2	Fw.	GTCCGCAAATGACCCCTTT
	Rev.	CCCACCCACTCTCTGACTTTC
m-Tmem26	Fw.	TCCTGTTGCATTCCCTGGTC
	Rev.	GGGTGCTGCAATACTGGTTTC
m-Adrb3	Fw.	GTCGTCTTCTGTGTAGCTACGGT
	Rev.	CATAGCCATCAAACCTGTTGAG
m-Lipe (m-Hsl)	Fw.	AGCCTCATGGACCCTCTTCT
	Rev.	AGCGAAGTGTCTCTCTGCAC
m-Atg (m-Pnpla2)	Fw.	ACTGAACCAACCCAACCCTT
	Rev.	CGCACTGGTAGCATGTTGGA
m-Olfr544	Fw.	CCTTATTGTCTTTGACTGCAACAT
	Rev.	TCGGTTGAAGATGCGAACAG
m-Pparg	Fw.	GCCCTTTGGTGACTTTATGGA
	Rev.	GCAGCAGGTTGTCTTGGATG
m-Chpt1	Fw.	TGTTCTGTGGATAGCAATGGTCA
	Rev.	GTCAATATGCTTGTAAACCTGTT
m-Cd206	Fw.	GTTCACCTGGAGTGATGGTTCTC
	Rev.	AGGACATGCCAGGGTCACCTTT
m-Cd163	Fw.	GGCTAGACGAAGTCATCTGCAC
	Rev.	CTTCGTTGGTCAGCCTCAGAGA
m-Nos2	Fw.	GAGACAGGGAAGTCTGAAGCAC
	Rev.	CCAGCAGTAGTTGCTCCTCTTC
m-Tnfa	Fw.	TGCCTATGTCTCAGCCTCTTC
	Rev.	GAGGCCATTTGGGAACTTCT
m-Il6	Fw.	GCTACCAAACTGGATATAATCAGGA
	Rev.	CCAGGTAGCTATGGTACTCCAGAA
m-Arg1	Fw.	CATTGGCTTGCGAGACGTAGAC
	Rev.	GCTGAAGGTCTCTTCCATCACC
m-Il4ra	Fw.	CACCTGGAGTGAGTGGAGTC
	Rev.	AGGCAAAACAACGGGATG
m-Lpcat2	Fw.	GTTGACCCTGACTCCCGAAAA
	Rev.	TGGGATGAAGGCTCCTGGTT
m-Pla2g2a	Fw.	AACTCCTGTCAGAAACGGCT
	Rev.	GTTTTCTTGTTCCGGGCGAA
m-Pla2g10	Fw.	ACATCCTGTGTGGTGAGTGC
	Rev.	TGGTCCACAAGGGTACAGGA
m-Pla2g7	Fw.	GAGCTAGTGTTGTGTGAGCCT
	Rev.	CTGACTCCCGGATACCCAGA
m-Agmo	Fw.	CTTTCTTAGGAGTTGACTTTGGCTACT
	Rev.	TGTGCTGCCCAGAAAATATTAATC

m-Npffr1	Fw.	CCCCCGAGTCTGAACGAGA
	Rev.	TAGTAGGAAGAGAAGGTGAGGCT
m-Npffr2	Fw.	CAGATTCCGCTGTGTGGTCT
	Rev.	TCGCTCTCAGGGAATAGGCT
m-Ppia	Fw.	ATTTCTTTTGACTTGCGGGC
	Rev.	AGACTTGAAGGGGAATG
m-Fabp4	Fw.	GAAATCACCGCAGACGACAG
	Rev.	AACTCTTGTGGAAGTCACGCC
m-Id3	Fw.	CTGCTACGAGGCGGTGTG
	Rev.	CACCTGGCTAAGCTGAGTGC
h-BACTIN	Fw.	AGAGCTACGAGCTGCCTGAC
	Rev.	AGCACTGTGTTGGCGTACAG
h-AGMO	Fw.	CTGACCTTGACTTCCATTGGATT
	Rev.	CAAGCAACGGAGAGTTTCCATA
h-CCL2	Fw.	CCTTCATTCCCCAAGGGCTC
	Rev.	GGTTTGCTTGTCCAGGTGGT
h-IL6	Fw.	GAGCAGGCACCCCAGTTAAT
	Rev.	ATTTGTGGTTGGGTCAGGGG
h-ILR4	Fw.	TTGCGAGTGGAAGATGAATG
	Rev.	CTCCGTTGTTCTCAGGGATAC
h-UCP1	Fw.	TGGAATAGCGGCGTGCTTG
	Rev.	CTCATCAGATTGGGAGTAG

PLA2G2A primer was obtained from Qiagen, #PPH05823B. Further tested primer sequences are available upon request.

Taqman probes

Gene	**Primer**	**Probe**
UCP1	F 5′- ACGACACGGTCCAGGAGTTC-3` R 5′- ACCAGCTAAAATCTTGCTTCCTAAAC-3`	5′-TCACCGCAGGGAAAGAAACAGCACC-3′
HPRT1	F 5′- GGCAGTATAATCCAAAGATGGTCAA R 5′- GTCTGGCTTATATCCAACACTTCGT	5′-CAAGCTTGCTGGTGAAAAGGACCCC-3′
ACTB	F 5′- CGACGCGGCTACAGCTT R 5′- CCTTAATGTCACGCACGATTT	5′-ACCACCACGGCCGAGCGG-3′
TBP	F 5′- TTGTAAACTTGACCTAAAGACCATTGC R 5′- TTCGTGGCTCTCTTATCCTCATG	5′-AACGCCGAATATAATCCCAAGCGGTTG-3′

Supplemental Table 4. Antibodies used in this study

UCP1	rabbit polyclonal Abcam, Cambridge, UK, ab10983; and rabbit polyclonal, Invitrogen, Carlsbad, California, PA1-24894
LPCAT2	rabbit polyclonal, Invitrogen, Carlsbad, California, PA5-52481
CHPT1	rabbit polyclonal, Invitrogen, Carlsbad, California, PA5-23695
PLA2G2A	sheep polyclonal, Invitrogen, Carlsbad, California, PA5-47672
PLA2G10	rabbit polyclonal, Invitrogen, Carlsbad, California, PA5-59776
F4/80 antigen	rabbit polyclonal, Santa Cruz Biotechnology, Dallas, Texas, sc-25830
PLA2G7	rabbit polyclonal, MyBioSource, San Diego, California, MBS9205733
AGMO	rabbit polyclonal, Aviva Systems Biology, San Diego, California ASB-ARP44468_P050
pSTAT6 and STAT6	rabbit polyclonal, Cell Signaling Technology, Danvers, Massachusetts, #9362, #9131
Phospho-p38 MAPK (Thr180, Tyr182)	APC, eBioscience, Thermofisher, Waltham, Massachusetts, clone: 4NIT4KK
Rabbit anti-goat IgG	H+L, cross-Adsorbed, FITC, polyclonal, secondary antibody, Invitrogen, Carlsbad, California, F-2765
Goat anti-rabbit IgG	H+L, HRP, Polyclonal, Secondary Antibody, Invitrogen, Carlsbad, California
Apoptosis detection	Invitrogen™ eBioscience™ Annexin V Apoptosis Detection Kit APC
Macrophage detection	F4/80 APC, CD45 PerCy5.5, CD11b APC or PE or AF700, CD68 PE or APC, Ki67 PE as detailed in (26); eBioscience, Thermofisher, Waltham, Massachusetts CD163 (10D6, Invitrogen, MA5-11458), Iba1 (Waco Chemicals, Richmond, VA, 019-19741)

Supplemental Methods

Analysis of AKGs

AKG species were analyzed by nano-electrospray ionization tandem mass spectrometry (Nano-ESI-MS/MS) with direct infusion of the lipid extract (Shotgun Lipidomics): tissue samples were weighed and homogenized in Milli-Q water (1 mg/10 µl) using the Precellys 24 Homogenizer (Peqlab) at 6,500 rpm for 30 sec. Body fluids (plasma, milk) were diluted with a 10-fold volume of water. Mouse milk was collected from the gastric content of neonate mice on PD3 and PD6, and used for subsequent analysis. Blood plasma was collected in EDTA-coated hemotubes and centrifuged at 1500 rpm for 15 min. In total, 50–200 µl of the tissue homogenate/diluted body fluid was used for extraction.

Before extraction, 200 ng of the internal standard 17:0 AKG (abcr Gmbh, Karlsruhe, Germany) was added to the tissue homogenate and body fluid samples; total lipids were then extracted using a method developed by Bligh & Dyer (44). The total lipid extract was dried under a constant stream of nitrogen. The dried lipid extract was resolved in 1.2 ml of methanol, and then 300 µl of 35 % potassium hydroxide in water was added. Alkaline hydrolysis was carried out for 1.5 hours at 80°C. The hydrolysate was extracted with 4 ml of hexane, which was then washed with 2 ml of water. The organic phase was dried under a stream of nitrogen, resolved in 100 µl of methanol and stored at -20 °C until analysis.

For analysis, the sample was diluted 1:4 with 10 mM ammonium acetate in methanol. Lipid infusion and ionization was conducted using Nano-ESI chips with the TriVersa NanoMate operated by ChipSoft Software (Advion) under the following settings: sample infusion volume: 14 µl, volume of air to aspirate after sample: 1 µl, air gap before chip: enabled, aspiration delay: 0 s, pre-piercing: with mandrel, spray sensing: enabled, cooling temperature: 10°C, gas pressure: 0.5 psi, ionization voltage: 1.4 kV, and vent headspace: enabled. Pre-wetting was done once. Mass spectrometric analysis was performed using the QTRAP 6500 (SCIEX) platform operated by Analyst 1.6.3.

The following instrument-dependent settings were used: curtain gas, 30 psi; CAD gas, medium; and interface heater temperature, 100°C. AKG analysis was performed in the positive ion mode by applying characteristic multiple reaction monitoring (MRM) transitions with additional scans for precursors of m/z 75 and m/z 93 for confirmation.

For quantification of AKG species, MRM data were processed using MultiQuant Software 3.0 (SCIEX). For each analyte, 3 MRMs were recorded, and the respective quantifier transition (see Table 1) was used for quantification. Endogenous AKG species were quantified against external calibration curves, which were calculated from MS/MS measurements of serially diluted synthetic AKG species in a range 1–250 µM. A fixed amount of the internal standard 17:0 AKG was added to each dilution. The standard calibration curves were plotted based on molar concentration *versus* peak area ratio of AKG species to the internal standard. Linearity and the correlation coefficient (R2) of the calibration curves were obtained *via* linear regression analysis. The calculated amounts of endogenous AKG species were normalized to the tissue weight or volume of body fluid, respectively.

Artificial rearing of neonate mice

Pregnant CD-1 mice (CLEA Japan, Inc., Tokyo, Japan) were bred on custom pelleted diets (MF, Oriental Yeast Co., Ltd., Tokyo, Japan, Supplemental Table 4), and male offspring were used in this study. The mice were maintained on the pelleted diet after weaning.

Supplemental Table 5. Composition of experimental diet[1]

Component	Amount (g/100 g diet)
Crude protein	23.1
Carbohydrates	55.3
Minerals	5.8
Crude fat	5.1
Dietary fiber	2.8

[1] The experimental diet was MF, obtained from Oriental Yeast Co., Tokyo, Japan.

Artificial rearing system

The artificial rearing procedure used a hand-feeding technique with specially-constructed nursing bottles. Pups were separated from their dams on postnatal day 2 and fed artificial milk by hand using a nursing bottle every 3 h (5 times/day). Pups were capable of suckling from silicon nipples connected to the nursing bottles. Pups were placed in a cage with an ovariectomized foster mother for maternal care and warmth except at feeding times. From day 14, pups were fed artificial milk from a nursing bottle in combination with a pelleted diet. Infant diets were made by mixing a crushed control diet and its respective artificial milk. Pups in all groups were weaned to the pelleted diet at day 21. Pups were housed in an artificially regulated environment at 23 ± 3°C, 55 ± 10% humidity using a 12-h light/dark cycle (lights on between 07:00-19:00).

Artificial mouse milk

Artificial milk formula was developed based on the methods of Hatanaka et al. (45), with slight modifications of fat content (Supplemental Table 5). Casein and whey protein were used as protein sources and lactose was used as the carbohydrate. Fat was adjusted to 16% by mixing several oils. For complete dissolution, ingredients were mixed using a sonicator (Ultrasonic Processor S-4000, Misonix, Inc., Farmingdale, NY). Milk was homogenized twice under high pressure (800–1000 bar) using a high-pressure homogenizer (Panda PLUS 2000, Niro Soavi S.p.A., Parma, Italy) resulting in emulsified, sterilized, and smoothed milk. The homogenized milk was stored at -80°C. AKG supplementation restored the natural AKG content of the milk (see Supplemental Figure 3E).

Supplemental Table 6. Composition of the artificial milk[1]

Ingredient		Amount (weight/100 ml milk)
Protein (g)	Whey protein isolate (BIPRO) [a]	4.0
	Whey protein hydrolyzed (PEPTIGEN® IF-3090) [b]	5.0
	Casein (Acid Casein LACTIC CASEIN720) [c]	4.0
	Serine [d]	0.02875
	Cystine [d]	0.3
	Tryptophan [d]	0.027
	Methionine [d]	0.0045
Carbohydrate (g)	Lactose [e]	1.89
Minerals (mg)	NaOH [d]	25
	KOH [e]	150
	$GlyCaPO_4$ [d]	800
	$MgCl_2$ $6H_2O$ [d]	190
	$CaCl_2$ $2H_2O$ [d]	170
	$CaCo_3$ [d]	184
	Ca-Citrate [e]	120
	Na_2HPO_4 [d]	80
	KH_2PO_4 [d]	8
	$FeSO_4$ [d]	24
	Citrate H_2O [e]	0.5
	$ZnSO_4$ [e]	6
	$CuSO_4$ [e]	1.5
	$MnSO_4$ [e]	0.25
	NaF [d]	0.155
	KI [d]	0.25
	K_2SO_4 [e]	163.5
	Na_2SiO_3 $9H_2O$ [d]	5.075
	Na_2O_4Se [d]	0.035
	$H_8MoN_2O_4$ $4H_2O$ [e]	0.0275
	$KCr(SO_4)_2$ $12H_2O$ [d]	0.975
	LiCl [e]	0.05
	H_3BO_3 [d]	0.285
	$NiCO_3$ [d]	0.1125
	NH_4VO_3 [e]	0.0225
Vitamins (mg)	Vitamin mix [f]	400
	Vitamin C [e]	200
	Vitamin K3 [d]	1.9825
	Vitamin A [e]	0.1284
	Vitamin D [d]	23.46
	Vitamin E [d]	0.0025
Others (mg)	Carnitine [d]	4
	Picolinate [d]	2
	Ethanolamine [d]	3.5
	Taurine [d]	15
	Tricholine citrate [d]	147
Fat (g)	(16.04 g)	
	MCT [g]	1.25
	Palm oil [h]	7.75
	Coconut oil [e]	2.5
	Corn oil [e]	none
	Soybean oil [e]	2.75
	Linseed oil [e]	0.75
	ARASCO® i	0.5
	DHASCO® I	0.5
	Cholesterol [e]	0.04

Component sources were as follows: [a]Davisco Foods International, Inc., Eden Prairie, MN; [b]Arla Foods Ingredients, Viby, Denmark; [c]Fonterra Co-operative Group Ltd., Auckland, New Zealand; [d]Sigma-Aldrich Corp., St. Louis, MO; [e]Wako Pure Chemical Industries, Ltd., Osaka, Japan; [f]Oriental Yeast Co., Ltd., Tokyo, Japan, [g]The Nisshin Oillio Group, Ltd., Tokyo, Japan; [h]Spectrum Laboratory Products, Inc., New Brunswick, NJ; [i]DSM Nutritional Products, Columbia, MD., MCT, medium-chain triglyceride.

Chemicals used for cell culture treatments

PAF C16:0, PAF C18:0, PAF C18:1 (50 nM, Cayman Chemicals, Ann Arbor, MI), carbamyl PAF (50 nM Merck, Sigma-Aldrich), azelaoyl PAF (50 nM Merck, Sigma-Aldrich, St. Louis, MO), rosiglitazone (1 μM Merck, Sigma-Aldrich, St. Louis, MO), IL-4 (10 ng/ml, 100 ng/ml for western blotting, Merck, Sigma-Aldrich), 10 ng/ml IL-10 (Immuno Tools GmbH, Friesoythe, Germany), IL-10 neutralizing antibody (1:10, eBioscience, Thermofisher), STAT6 inhibitor (AS1517499, 200 nM, Axon Medchem, Groningen The Netherlands, details of utilization described before (26)), PTAFR inhibitor SR27417 (10 nM, Merck, Sigma-Aldrich, St. Louis, MO), PPARγ inhibitor GW9662 (10 μM Merck, Sigma-Aldrich, St. Louis, MO), STAT3 inhibitor cucurbitacin I (500 nM, Cayman Chemicals, Ann Arbor, MI), JAK/STAT3 inhibitor ruxolitinib (280 nM, Cayman Chemicals, Ann Arbor, MI), farnesol (100 nM, Merck, Sigma-Aldrich, St. Louis, MO), TSI-01 (0.5 μM), LY315920 (9 nM), sPLA2 inhibitor 17277 (1 nM, all from Cayman Chemicals), IL-6 (0.2 ng/ml, Merck Sigma-Aldrich, St. Louis, MO), TNFα (50 pg/ml, Merck Sigma-Aldrich, St. Louis, MO).

Samples from non-human primates

Samples of visceral AT of neonate Rhesus monkey *(Macaca mulatta)* were collected and provided by the Wisconsin National Primate Research Center. Case identifiers: 2016c331, 2016c270, 2017c349. Antibodies for ATM labeling were used as reported before for other tissue resident macrophages in Rhesus monkey (46, 47).

Bone marrow derived macrophage differentiation

We differentiated macrophages from bone marrow progenitors of wild-type and PTAFR-deficient *(Ptafr$^{-/-}$)* mice, and used them for subsequent treatment with AKGs. The *in vitro* macrophage differentiation protocol was described before (26).

ELISA assays

We used commercial ELISA kits to measure the level of PAF, lyso-PAF, AGMO, 15-deoxy-delta 12,14-prostaglandin J2 (all from MyBioSource, San Diego, CA), IL-6, TNFα (Fisher Scientific, Hampton, NH) prostaglandin D2 (Abcam, Cambridge, UK), STAT3 and pSTAT3 (Biocat GmbH, Heidelberg, Germany), NPFF (Cloud-Clone Corp., Wuhan, PRC). We used colorimetric methods to determine glycerol (Merck, Sigma-Aldrich, St. Louis, MO) and TG level (Fluitest TG, Analyticon, Lichtenfels, Germany), according to the manufacturer´s instructions. Uncoupled mitochondrial respiration (NADH-DH activity) was measured with WST-81 assay (Carl Roth, Karlsruhe, Germany) and normalized to mitochondrial content assayed with Mitotracker Green, and expressed relative to vehicle value.

Heat imaging

A thermographic camera (FLIR Systems, Inc) was used to acquire images of neonate mice, before the development of fur, which would interfere with measurement. Mice were placed on ambient temperature flat restrainers, and images were taken immediately, using a 60 cm surface distance.

Adipocyte differentiation *in vitro*

Preadipocytes of the stromal vascular fraction were isolated and maintained as described before (26, 27, 48) (Supplemental Figure 7A). To ensure ATM depletion from the harvested preadipocytes, we used magnetic bead cell purification of the stromal vascular fraction with an antibody against F4/80 antigen (Miltenyi Biotec, Bergisch Gladbach, Germany). Preadipocytes were maintained in cell culture media supplemented with 20 µg/ml insulin; for white adipocyte development, we treated the cells with 50 µM IBMX, 1 µM dexamethasone, 1 µM rosiglitazone, 20 µg/ml insulin as described before (49) (Supplemental Figure 7B). To induce beige differentiation of preadipocytes of the stromal vascular fraction, we used the same treatment, complemented with 50 nM triiodothyronine and 10 µM isoproterenol (all from Merck Sigma-Aldrich), as described before (50).

Mito Thermo Yellow labeling of mitochondria

Mito Thermo Yellow (MTY), a temperature sensitive fluorescent probe (51) was used to assess increased mitochondrial thermogenesis, and uncoupling, as described before (52, 53). MTY was developed and provided by Dr. Y.-T. Chang (Center for Self-assembly and Complexity, Institute for Basic Science (IBS) & Department of Chemistry, Pohang University of Science and Technology (POSTECH), Pohang 37673, Republic of Korea). We used MTY for FACS analysis, at a 0.1 ng/ml concentration to label 10^6/ml cells. Cells were kept at 37°C throughout the assay

Oxygen consumption assay and flow cytometry analysis of mitochondrial biogenesis

To measure oxygen consumption, as an indicative of increased mitochondrial content (54), we plated 3T3-L1 cells into 96-well culture plates, suitable for fluorescent plate reader. Cells were cultured in L-15 medium with glutamate (Merck Sigma-Aldrich), supplemented with 10% FCS and 1% penicillin/streptomycin. After reaching confluence, adipocyte differentiation was induced, as described above. Cells were treated with conditioned media of ATMs for 18 h, or with vehicle or AKGs for 18 h. Oxygen consumption was assayed with Extracellular O_2 Consumption Reagent (ab197242, AbCam), for 30-120 min, according to the manufacturer´s protocol. We used a CLARIO Star (BMG Labtech) fluorescent plate reader for signal detection. Signal was normalized to total cellular protein content. Mitochondrial biogenesis was detected with MitoBiogenesis™ Flow Cytometry Kit (AbCam), using the manufacturer´s protocol.

Indirect calorimetry

Respiratory exchange rate (RER), oxygen consumption (VO_2) and energy expenditure (EE) were measured in each individual mouse for 24 h using a small animal indirect calorimetry system (CaloBox, Phenosys, Germany). Mean RER, VO_2 and EE values were determined over 7 h in the middle of both the day-, and the night phases. For this assay we used male C57BL/6 obese mice, fed with a HFD, and treated with vehicle or AKGs.

Overexpression studies

For overexpressing *Agmo* mouse tagged ORF clone (NM178767) and *Lpcat2* mouse tagged ORF clone (NM173014) was overexpressed in J774A.1 cells. Briefly, 1.2 µg of DNA was transfected to 300.000 cells, using TurboFect Transfection Reagent (Fisher Scientific, Hampton, NH) according to the manufacturer´s instructions. Control cells received empty pCMV6 entry vector. Analyses were carried out 24 h after transfection.

Oil red-O staining, quantification of UCP1 staining

TG content of cultured adipocytes were stained with oil red-O, as described before (26). UCP1 immunostained samples were photographed and optical density of the images were measured with digital image analysis. Original images are available upon request through Figshare.

Transmission electron microscopy (TEM)

Cells were fixed in paraformaldehyde/glutaraldehyde, and processed for TEM analysis as described before (27).

Cell viability assay

We used Presto Blue cell viability assay (Thermofisher, Waltham, MA) and Rotitest Vital (Carl Roth, Karlsruhe, Germany) cell viability assays, according to the manufacturers´ instructions.

BeAT image analysis software is available under the following link

https://drive.google.com/open?id=1HoQVYG4ofWmNmc9p9imKkUyEkWveQndd

A tutorial is available in YouTube: https://www.youtube.com/watch?v=Nbctef3Qrug

Acknowledgements for the supplementary information

Research reported in this publication was supported in part by the Office of the Director, National Institutes of Health under Award Number P51OD011106 to the Wisconsin National Primate Research Center, University of Wisconsin-Madison. This research was conducted in part at a facility constructed with support from Research Facilities Improvement Program grant number RR15459-01 and RR02014-01. The content is solely the responsibility of the authors and does not necessarily represent the official views of the National Institutes of Health. Prof. Hartmut Geiger (University of Ulm) provided access to FACS equipment. Assistance of Carina Preischl (Oil red-O staining and mRNA analysis in differentiating 3T3-L1 cells), and Tanmay Sadhanasatish in image analysis is appreciated. The macrophage artwork used in the graphical abstract and in Figure 7F was provided by Dreamstime Stock Photography.

Supplementary References

1. Gouon-Evans V, Lin EY, and Pollard JW. Requirement of macrophages and eosinophils and their cytokines/chemokines for mammary gland development. *Breast Cancer Research : BCR.* 2002;4(4):155-64.
2. Koletzko B. Human Milk Lipids. *Ann Nutr Metab.* 2016;69 Suppl 2:12.
3. Hallgren B, Niklasson A, Stallberg G, and Thorin H. On the occurrence of 1-O-alkylglycerols and 1-O-(2-methoxyalkyl)glycerols in human colostrum, human milk, cow's milk, sheep's milk, human red bone marrow, red cells, blood plasma and a uterine carcinoma. *Acta Chem Scand B.* 1974;28(9):1029-34.
4. Hartvigsen K, Ravandi A, Harkewicz R, Kamido H, Bukhave K, Holmera G, et al. 1 -O-alkyl-2-(omega-oxo)acyl-sn-glycerols from shark oil and human milk fat are potential precursors of PAF mimics and GHB. *Lipids.* 2006;41(7):679-93.
5. Meimetis LG, Williams DE, Mawji NR, Banuelos CA, Lal AA, Park JJ, et al. Niphatenones, glycerol ethers from the sponge *Niphates digitalis* block androgen receptor transcriptional activity in prostate cancer cells: structure elucidation,

synthesis, and biological activity. *Journal of Medicinal Chemistry.* 2012;55(1):503-14.
6. McClintock JB, Baker BJ, Slattery M, Heine JN, Bryan PJ, Yoshida W, et al. Chemical defense of common antarctic shallow-water nudibranch *Tritoniella belli* Eliot (Mollusca: Tritonidae) and its prey, *Clavularia frankliniana* Rouel (Cnidaria: Octocorallia). *Journal of chemical ecology.* 1994;20(12):3361-72.
7. Santos VLCS, Billett DSM, and Wolff GA. 1-O-alkylglyceryl ether lipids of the gut walls and contents of an abyssal holothurian *(Oneirophanta mutabilis)*. *Journal of the Brazilian Chemical Society.* 2002;13:653-7.
8. Iannitti T, and Palmieri B. An update on the therapeutic role of alkylglycerols. *Mar Drugs.* 2010;8(8):2267-300.
9. Zhang M, Sun S, Tang N, Cai W, and Qian L. Oral administration of alkylglycerols differentially modulates high-fat diet-induced obesity and insulin resistance in mice. *Evid Based Complement Alternat Med.* 2013;2013:834027.
10. Ellingboe J, and Karnovsky ML. Origin of glycerol ethers. Biosynthesis from labeled acetate, stearic acid, stearaldehyde, and stearyl alcohol. *The Journal of biological chemistry.* 1967;242(24):5693-9.
11. Grossi V, Mollex D, Vinçon-Laugier A, Hakil F, Pacton M, and Cravo-Laureau C. Mono- and Dialkyl glycerol ether lipids in anaerobic bacteria: Biosynthetic insights from the mesophilic sulfate reducer *Desulfatibacillum alkenivorans*. *Applied and Environmental Microbiology.* 2015;81(9):3157-68.
12. Wang Y, and Xu Y. Distribution and source of 1-O-monoalkyl glycerol ethers in the Yellow River and Bohai Sea. *Organic Geochemistry.* 2016;91:81-8.
13. Ahrne L, and Palmquist DL. Incorporation of [hydrogen-3] alkylglycerolether and [carbon-14] hexadecanol into bovine colostrum and milk lipids. *Journal of dairy science.* 1982;65(10):1905-11.
14. Ahrne L, Bjorck L, and Claesson O. Alkylglycerols in bovine colostrum and milk in relation to precursor levels. *J Dairy Res.* 1983;50(2):201-6.
15. Qian L, Song H, Zheng T, Zhong Y, Yu W, Wu S, et al. Determination of alkylglycerol contents in breast milk. *J Clin Pediatr.* 2014;32(6):540-3.
16. Oswald EO, Anderson CE, Piantadosi C, and Lim J. Metabolism of alkyl glyceryl ethers in the rat. *Lipids.* 1968;3(1):51-8.
17. Hallgren B, and Larsson S. The glyceryl ethers in man and cow. *Journal of lipid research.* 1962;3(1):39-43.
18. Johnson W, Jr., Bergfeld WF, Belsito DV, Hill RA, Klaassen CD, Liebler D, et al. Safety assessment of alkyl glyceryl ethers as used in cosmetics. *International journal of toxicology.* 2013;32(5 Suppl):5S-21S.
19. Brites P, Ferreira AS, da Silva TF, Sousa VF, Malheiro AR, Duran M, et al. Alkyl-glycerol rescues plasmalogen levels and pathology of ether-phospholipid deficient mice. *PLoS One.* 2011;6(12):e28539.
20. Bergan J, Skotland T, Sylvänne T, Simolin H, Ekroos K, and Sandvig K. The ether lipid precursor hexadecylglycerol causes major changes in the lipidome of HEp-2 cells. *PLOS ONE.* 2013;8(9):e75904.
21. Cheminade C, Gautier V, Hichami A, Allaume P, Le Lannou D, and Legrand AB. 1-O-alkylglycerols improve boar sperm motility and fertility. *Biol Reprod.* 2002;66(2):421-8.
22. Wu S, and Zhang Y. LOMETS: a local meta-threading-server for protein structure prediction. *Nucleic acids research.* 2007;35(10):3375-82.
23. Watschinger K, Keller MA, McNeill E, Alam MT, Lai S, Sailer S, et al. Tetrahydrobiopterin and alkylglycerol monooxygenase substantially alter the murine macrophage lipidome. *Proc Natl Acad Sci U S A.* 2015;112(8):2431-6.

24. Watschinger K, and Werner ER. Orphan enzymes in ether lipid metabolism. *Biochimie.* 2013;95(1):59-65.
25. Tokuoka SM, Kita Y, Shindou H, and Shimizu T. Alkylglycerol monooxygenase as a potential modulator for PAF synthesis in macrophages. *Biochem Biophys Res Commun.* 2013;436(2):306-12.
26. Waqas SFH, Hoang A, Lin Y, Ampem G, et al, and Röszer T. Neuropeptide FF increases M2 activation and self-renewal of adipose tissue macrophages. *The Journal of Clinical Investigation* 2017;127(7):2842-54.
27. Waqas SFH, Noble A, Hoang A, Ampem G, Popp M, Strauß S, et al. Adipose tissue macrophages develop from bone marrow-independent progenitors in *Xenopus laevis* and mouse. *Journal of Leukocyte Biology.* 2017;102(3):845-55.
28. Hichami A, Duroudier V, Leblais V, Vernhet L, Le Goffic F, Ninio E, et al. Modulation of platelet-activating-factor production by incorporation of naturally occurring 1-O-alkylglycerols in phospholipids of human leukemic monocyte-like THP-1 cells. *Eur J Biochem.* 1997;250(2):242-8.
29. Galvão I. In: Riccardi C, Levi-Schaffer F, and Tiligada E eds. *Immunopharmacology and Inflammation*. Springer International Publishing; 2018:3-32.
30. Curfs DM, Ghesquiere SA, Vergouwe MN, van der Made I, Gijbels MJ, Greaves DR, et al. Macrophage secretory phospholipase A2 group X enhances anti-inflammatory responses, promotes lipid accumulation, and contributes to aberrant lung pathology. *The Journal of biological chemistry.* 2008;283(31):21640-8.
31. Hasegawa S, Kohro Y, Shiratori M, Ishii S, Shimizu T, Tsuda M, et al. Role of PAF Receptor in Proinflammatory Cytokine Expression in the Dorsal Root Ganglion and Tactile Allodynia in a Rodent Model of Neuropathic Pain. *PLOS ONE.* 2010;5(5):e10467.
32. Murase R, Sato H, Yamamoto K, Ushida A, Nishito Y, Ikeda K, et al. Group X secreted phospholipase a(2) releases ω3 polyunsaturated fatty acids, suppresses colitis, and promotes sperm fertility. *The Journal of biological chemistry.* 2016;291(13):6895-911.
33. Bergan J, Skotland T, Lingelem AB, Simm R, Spilsberg B, Lindback T, et al. The ether lipid precursor hexadecylglycerol protects against Shiga toxins. *Cell Mol Life Sci.* 2014;71(21):4285-300.
34. Sugatani J, Sadamitsu S, Yamaguchi M, Yamazaki Y, Higa R, Hattori Y, et al. Antiobese function of platelet-activating factor: increased adiposity in platelet-activating factor receptor-deficient mice with age. *FASEB journal : official publication of the Federation of American Societies for Experimental Biology.* 2014;28(1):440-52.
35. Kuefner MS, Pham K, Redd JR, Stephenson EJ, Harvey I, Deng X, et al. Secretory phospholipase A2 group IIA modulates insulin sensitivity and metabolism. *Journal of lipid research.* 2017;58(9):1822-33.
36. Peek CB, Affinati AH, Ramsey KM, Kuo HY, Yu W, Sena LA, et al. Circadian clock NAD+ cycle drives mitochondrial oxidative metabolism in mice. *Science.* 2013;342(6158):1243417.
37. Dagda RK, Cherra SJ, Kulich SM, Tandon A, Park D, and Chu CT. Loss of PINK1 function promotes mitophagy through effects on oxidative stress and mitochondrial fission. *The Journal of biological chemistry.* 2009;284(20):13843-55.
38. Eide GE, Roelants M, Bjerknes R, and Júlíusson PB. BMI and BMI SDS in childhood: annual increments and conditional change AU - Brannsether, Bente. *Annals of Human Biology.* 2017;44(1):28-33.
39. Sacco MR, de Castro NP, Euclydes VL, Souza JM, and Rondo PH. Birth weight, rapid weight gain in infancy and markers of overweight and obesity in childhood. *Eur J Clin Nutr.* 2013;67(11):1147-53.

40. Kromeyer-Hauschild K, Wabitsch M, Kunze D, Geller D, Geiss HC, Hesse V, et al. *Percentiles of body mass index in children and adolescents evaluated from different regional German studies. Monatsschrift Kinderheilkunde.* 2001.
41. WHO. Global Database on Child Growth and Malnutrition. https://www.who.int/nutgrowthdb/about/introduction/en/index4.html.
42. de Onis M, Monteiro C, Akre J, and Glugston G. The worldwide magnitude of protein-energy malnutrition: an overview from the WHO Global Database on Child Growth. *Bulletin of the World Health Organization.* 1993;71(6):703-12.
43. Sorva R, Tolppanen EM, Lankinen S, and Perheentupa J. Growth evaluation: parent and child specific height standards. *Archives of disease in childhood.* 1989;64(10):1483-7.
44. Bligh EG, and Dyer WJ. A rapid method of total lipid extraction and purification. *Canadian Journal of Biochemistry and Physiology.* 1959;37(8):911-7.
45. Hatanaka E, Harauma A, Yasuda H, Watanabe J, Nakamura MT, Salem N, Jr., et al. Essentiality of arachidonic acid intake in murine early development. *Prostaglandins, leukotrienes, and essential fatty acids.* 2016;108:51-7.
46. Cai Y, Sugimoto C, Arainga M, Alvarez X, Didier ES, and Kuroda MJ. In vivo characterization of alveolar and interstitial lung macrophages in Rhesus macaques: implications for understanding lung disease in humans. *Journal of immunology.* 2014;192(6):2821-9.
47. Smith KA, Pearson CB, Hachey AM, Xia DL, and Wachtman LM. Alternative activation of macrophages in rhesus macaques *(Macaca mulatta)* with endometriosis. *Comparative medicine.* 2012;62(4):303-10.
48. Hausman DB, Park HJ, and Hausman GJ. Isolation and culture of preadipocytes from rodent white adipose tissue. *Methods in molecular biology.* 2008;456:201-19.
49. Zebisch K, Voigt V, Wabitsch M, and Brandsch M. Protocol for effective differentiation of 3T3-L1 cells to adipocytes. *Analytical biochemistry.* 2012;425(1):88-90.
50. Wu J, Bostrom P, Sparks LM, Ye L, Choi JH, Giang AH, et al. Beige adipocytes are a distinct type of thermogenic fat cell in mouse and human. *Cell.* 2012;150(2):366-76.
51. Arai S, Suzuki M, Park SJ, Yoo JS, Wang L, Kang NY, et al. Mitochondria-targeted fluorescent thermometer monitors intracellular temperature gradient. *Chemical communications.* 2015;51(38):8044-7.
52. Lane N. Hot mitochondria? *PLoS biology.* 2018;16(1):e2005113.
53. Chrétien D, Bénit P, Ha H-H, Keipert S, El-Khoury R, Chang Y-T, et al. Mitochondria are physiologically maintained at close to 50 °C. *PLoS biology.* 2018;16(1):e2003992.
54. Babaei R, Schuster M, Meln I, Lerch S, Ghandour RA, Pisani DF, et al. Jak-TGFβ cross-talk links transient adipose tissue inflammation to beige adipogenesis. *Science Signaling.* 2018;11(527).

Unedited, uncropped western blots

pSTAT6 (Supplemental Figure 11C)

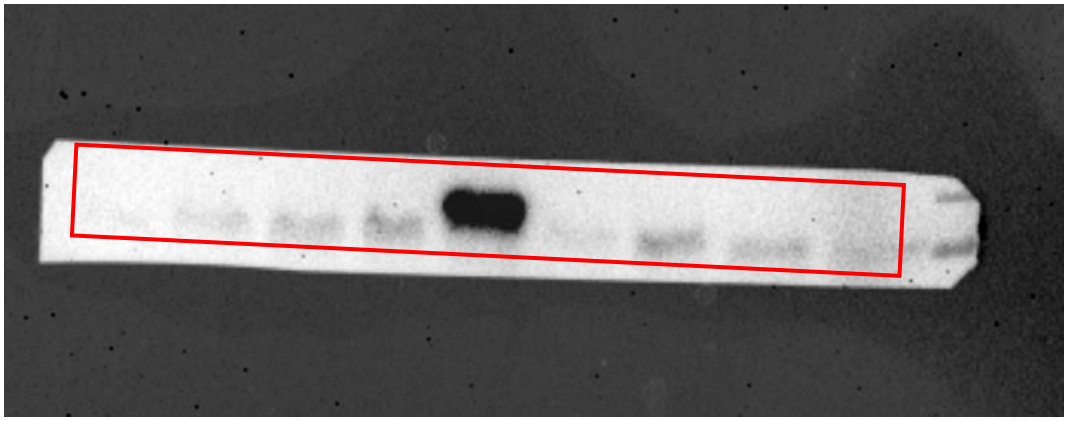

STAT6 (Supplemental Figure 11C)

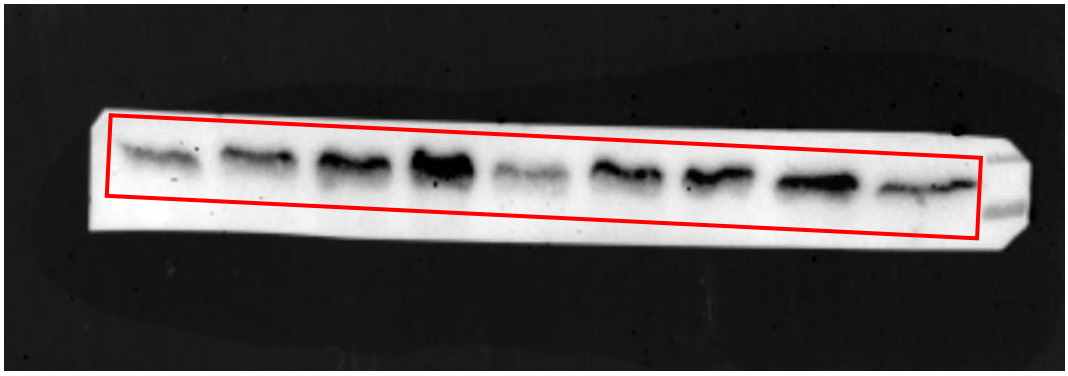

Beta-actin (Supplemental Figure 11C)

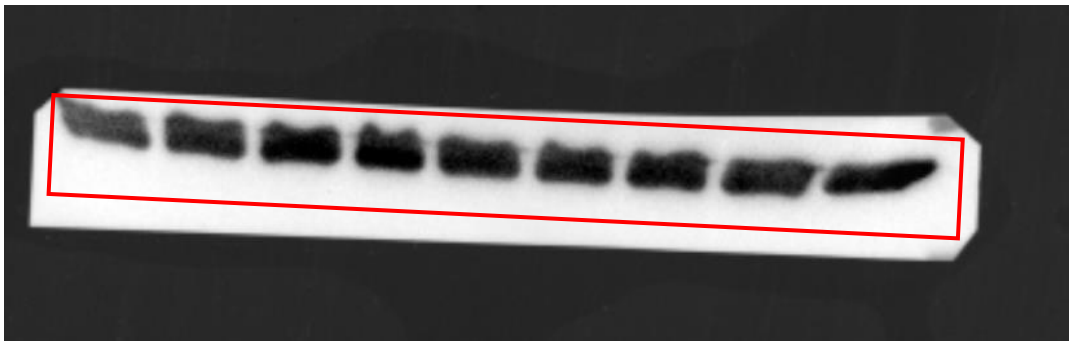

LPCAT2 (Supplemental Figure 13A)

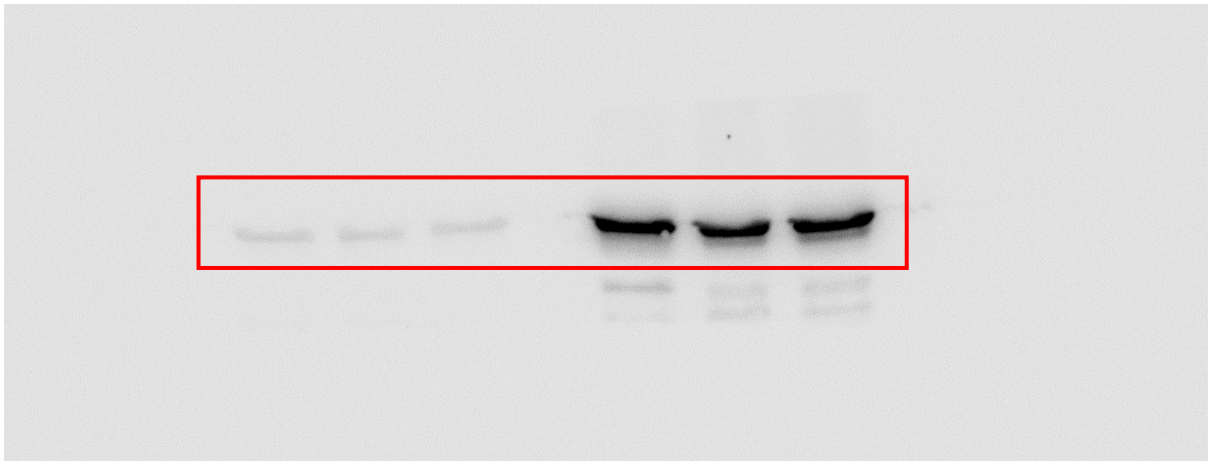

Beta-actin (Supplemental Figure 13A, LPCAT2 bands are still visible)

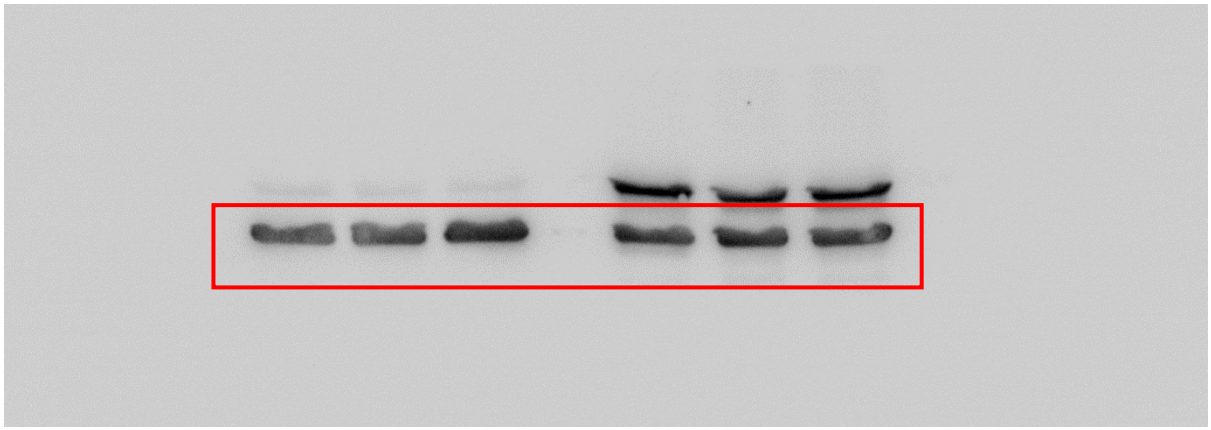

Corresponding membrane:

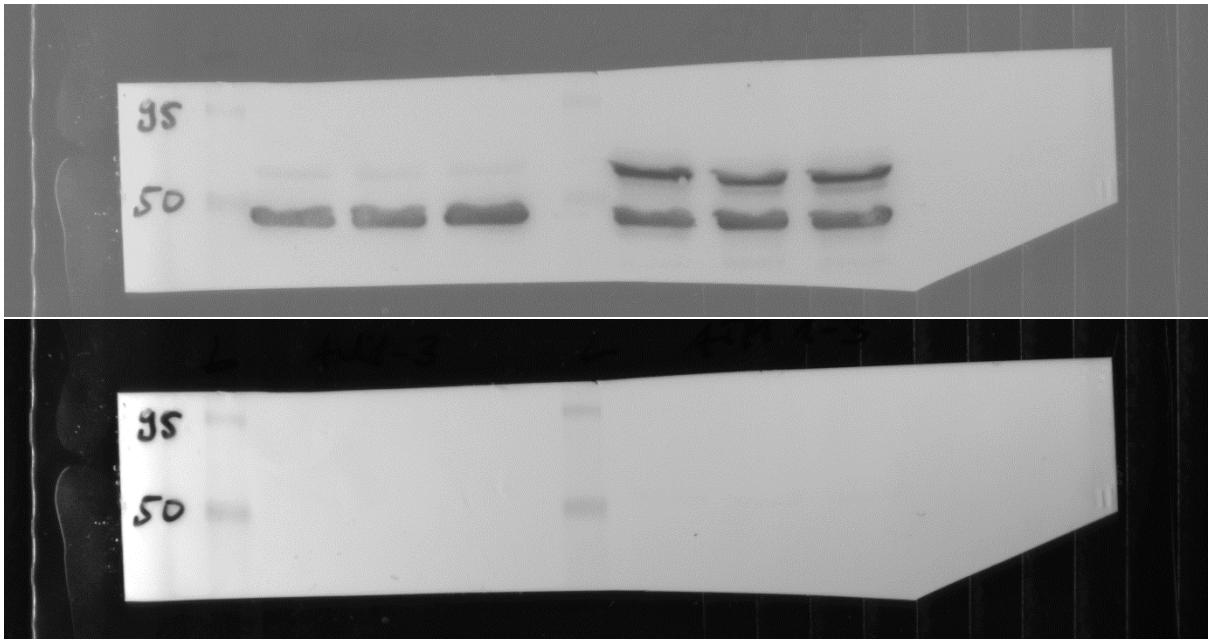

UCP1 (Supplemental Figure 16F)

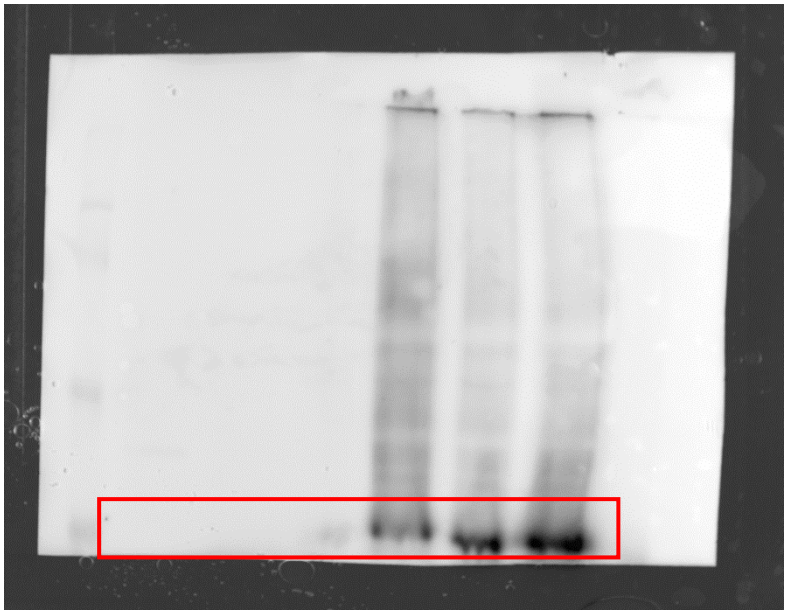

Beta-actin (Supplemental Figure 16F)

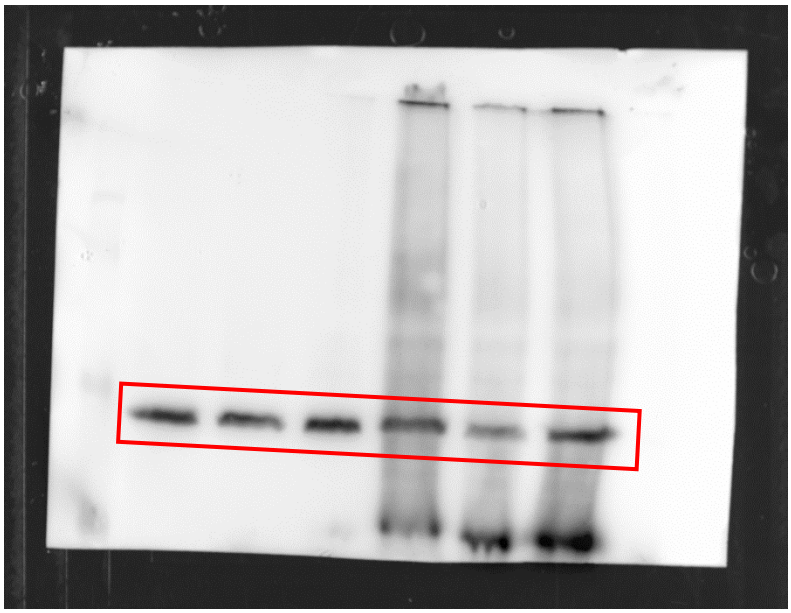

Further **UCP1** antibody tests, which are not shown in the Figures:

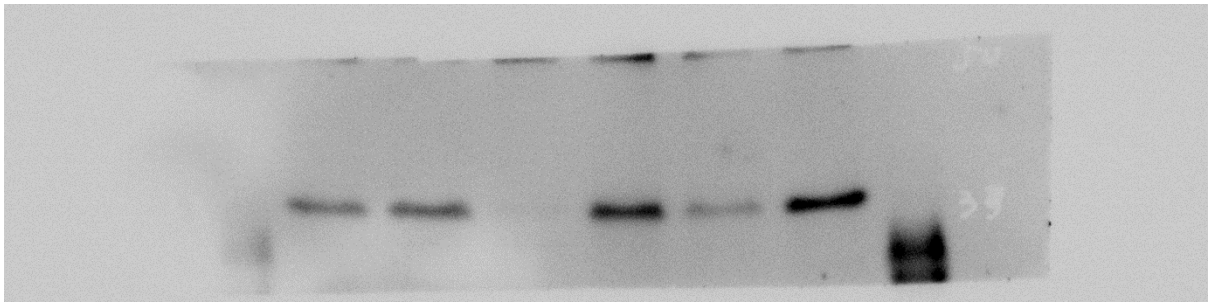

Corresponding beta-actin: